12-4-2013

Magnetic Inhibition of Convection and the Fundamental Properties of Low-Mass Stars. I. Stars with a Radiative Core

Gregory A. Feiden
Dartmouth College

Brian Chaboyer
Dartmouth College

The Astrophysical Journal, 779:183 (25pp), 2013 December 20 doi:10.1088/0004-637X/779/2/183

MAGNETIC INHIBITION OF CONVECTION AND THE FUNDAMENTAL PROPERTIES OF LOW-MASS STARS. I. STARS WITH A RADIATIVE CORE

Gregory A. Feiden[1] and Brian Chaboyer
Department of Physics and Astronomy, Dartmouth College, 6127 Wilder Laboratory, Hanover, NH 03755, USA;
gregory.a.feiden.gr@dartmouth.edu, brian.chaboyer@dartmouth.edu
Received 2013 August 20; accepted 2013 October 31; published 2013 December 4

ABSTRACT

Magnetic fields are hypothesized to inflate the radii of low-mass stars—defined as less massive than 0.8 $M_{\odot}$—in detached eclipsing binaries (DEBs). We investigate this hypothesis using the recently introduced magnetic Dartmouth stellar evolution code. In particular, we focus on stars thought to have a radiative core and convective outer envelope by studying in detail three individual DEBs: UV Psc, YY Gem, and CU Cnc. Our results suggest that the stabilization of thermal convection by a magnetic field is a plausible explanation for the observed model-radius discrepancies. However, surface magnetic field strengths required by the models are significantly stronger than those estimated from observed coronal X-ray emission. Agreement between model predicted surface magnetic field strengths and those inferred from X-ray observations can be found by assuming that the magnetic field sources its energy from convection. This approach makes the transport of heat by convection less efficient and is akin to reduced convective mixing length methods used in other studies. Predictions for the metallicity and magnetic field strengths of the aforementioned systems are reported. We also develop an expression relating a reduction in the convective mixing length to a magnetic field strength in units of the equipartition value. Our results are compared with those from previous investigations to incorporate magnetic fields to explain the low-mass DEB radius inflation. Finally, we explore how the effects of magnetic fields might affect mass determinations using asteroseismic data and the implication of magnetic fields on exoplanet studies.

Key words: binaries: eclipsing – stars: evolution – stars: interiors – stars: low-mass – stars: magnetic field

Online-only material: color figures

1. INTRODUCTION

Magnetic fields are a ubiquitous feature of stars across the Hertzsprung–Russell diagram. Despite their ubiquity, magnetic fields have often been excluded from low-mass stellar evolutionary calculations as there has been little need for their inclusion. Recently, however, observations of low-mass stars—here defined to have $M < 0.8\,M_{\odot}$—in detached eclipsing binaries (DEBs) have altered this perception; magnetic fields might be necessary after all (Ribas 2006; López-Morales 2007). We began an effort to address this necessity in a previous paper, where we described a new stellar evolution code that includes effects due to magnetic perturbations (Feiden & Chaboyer 2012b). A single case study provided an initial assessment of the code's viability, but did not specifically investigate the problems with low-mass stars. Here, we investigate the hypothesis that magnetic field effects are required to accurately model low-mass stars.

The geometry of DEBs permits a nearly model independent determination of the fundamental properties (mass, radius, effective temperature) of the constituent stars (see the reviews by Popper 1980; Andersen 1991; Torres et al. 2010). Stellar masses and radii can typically be determined with a precision below 3% given quality photometric and spectroscopic observations (Andersen 1991; Torres et al. 2010).[2] This permits rigorous tests of stellar evolution theory. Any disagreements between observations and stellar evolution models become strikingly apparent.

Observations show that stellar evolution models routinely predict radii about 5% smaller than real stars, at a given mass (see, e.g., Torres & Ribas 2002; Ribas 2006; Morales et al. 2008, 2009; Torres et al. 2010; Kraus et al. 2011; Irwin et al. 2011; Doyle et al. 2011; Winn et al. 2011). Star-to-star age and metallicity variations may account for some, but not all, of the noted discrepancies (Feiden & Chaboyer 2012a; Torres 2013). However, the problem appears to be exacerbated by more well-studied systems, which exhibit near 10% radius discrepancies (Popper 1997; Feiden & Chaboyer 2012a; Terrien et al. 2012). To further complicate the matter, seemingly hyper-inflated stars show radii inflated by more than 50% (Vida et al. 2009; Çakırlı et al. 2010, 2013a, 2013b; Ribeiro et al. 2011). Whether the mechanism puffing up the hyper-inflated stars is related to the more common sub-10% inflation is unclear. Regardless, numerous low-mass stars show significant departures from radius predictions of standard stellar evolution theory.

In addition to the radius discrepancies, effective temperatures ($T_{\rm eff}$s) predicted by stellar evolution models are inconsistent with observations. Observations indicate that low-mass stars tend to be 3%–5% cooler than theoretical predictions (Torres et al. 2010). However, this problem is complicated by the fact that absolute $T_{\rm eff}$ measurements for stars in DEBs are subject to significant uncertainty (Torres et al. 2010; Torres 2013). DEB geometry only allows for an accurate determination of the temperature ratio. Difficulty in determining absolute $T_{\rm eff}$s has garnered support from a noted discrepancy in the radius–$T_{\rm eff}$ relation between single field stars and stars in DEBs (Boyajian et al. 2012). Whether this discrepancy is indicative of an innate

[1] Current address: Department of Physics and Astronomy, Uppsala University, Box 516, Uppsala 751 20, Sweden.
[2] One must be mindful that larger systematic uncertainties may be lurking in the data (Morales et al. 2010; Windmiller et al. 2010).

difference between single field stars and stars in DEBs, or highlights errors in the determination of $T_{\rm eff}$ in either population is debatable. As a result, mass-$T_{\rm eff}$ discrepancies have not received as much attention in the literature as the mass-radius problem. We will continue this trend and use the mass-radius relation as a primary guide for testing stellar models. DEB $T_{\rm eff}$s will be consulted only for additional guidance.

Other areas of astrophysics are impacted by the inaccuracies of stellar evolution models. With typical lifetimes greater than a Hubble time (Laughlin et al. 1997), low-mass stars are excellent objects for studying galactic structure and evolution (e.g., Reid et al. 1995; Fuchs et al. 2009; Pineda et al. 2013). The history of the galaxy is effectively encoded within the population of low-mass stars. Understanding their properties allows for this history to be constructed. Their low-mass, small radius, and faint luminosity also provides an advantage for observers searching Earth-sized planets orbiting in their host star's habitable zone (Charbonneau 2009; Gillon et al. 2010). Significant effort is being devoted to hunting for and characterizing planets around M-dwarfs (e.g., Nutzman & Charbonneau 2008; Quirrenbach et al. 2010; Muirhead et al. 2012; Mahadevan et al. 2012; Dressing & Charbonneau 2013). These applications require an intimate understanding of how physical observables of M-dwarfs are influenced by the star's fundamental properties and vice versa. It is therefore prudent to look closely at the problems presented by stars in DEBs to better comprehend the impact of a star's physical "ingredients" on its observable properties.

The leading hypothesis to explain the model-observation radius discrepancies is the presence of magnetic fields (Mullan & MacDonald 2001; Ribas 2006; López-Morales 2007; Morales et al. 2008). Many stars that display inflated radii exist in short period DEBs whose orbital periods are less than 3 days. Stars in short period DEBs will have a rotational period synchronized to their orbital period by tidal interactions with their companion (Zahn 1977). At a given main-sequence (MS) age, stars in short period DEBs will be rotating faster than a comparable single field star. Since the stellar dynamo mechanism is largely driven by rotation, tidal synchronization allows a star to produce and maintain a strong magnetic field throughout its MS lifetime.

However, radius deviations are not only observed among stars in short period systems. A number of long period DEBs have low-mass stars that display inflated radii (Irwin et al. 2011; Doyle et al. 2011; Winn et al. 2011; Bender et al. 2012; Orosz et al. 2012; Welsh et al. 2012). Stars in long period systems, even if they are rotationally synchronized, are presumed to be slow rotators. In two of these systems, LSPM J1112+7626 (Irwin et al. 2011) and Kepler-16 (Winn et al. 2011), this assumption has been confirmed. The primary star in LSPM J1112+7626 has an approximately 65 day rotation period inferred from out-of-eclipse light curve modulation, suggesting that it is both slow rotating and not rotationally synchronized. Kepler-16 A, on the other hand, was observed to have a rotation period of roughly 36 days from spectroscopic line broadening with minimal chromospheric activity apparent from Ca II observations (Winn et al. 2011).

Though these systems appear to refute the magnetic field hypothesis, little is known about the rotational characteristics of the secondary stars. If the stars are spinning down as single stars (Skumanich 1972), then it is possible that the secondary stars are still rotating rapidly enough to drive a strong dynamo. Low-mass stars appear to only require rotational velocities of order 3 km s^{-1} (rotation period of roughly 3 days) before they display evidence of magnetic flux saturation (Reiners et al. 2009). Furthermore, pseudo-synchronization may take place (Hut 1981). Numerous short tidal interactions at periastron can cause binary companions to synchronize with a period not quite equal to the orbital period (see, e.g., Winn et al. 2011). Thus, stars in long period DEBs do not necessarily evolve as if they were isolated, potentially exciting the stellar dynamo. However, each of the above circumstances do not appear sufficient to explain the inflated radii of LSPM J1112+7626 B and Kepler-16 B. LSPM J1112 would be nearly 9 Gyr old given the rotation period of the primary, suggesting the secondary has also had ample time to spin down. Kepler-16 shows evidence for pseudo-synchronization, which would impart a rotation period of nearly 36 days onto the secondary, giving it a rotational velocity of below 0.5 km s^{-1}.

Support is lent to the magnetic field hypothesis by observations that low-mass DEBs exhibit strong magnetic activity. Inflated stars, in particular, often display strong chromospheric Hα emission (Morales et al. 2008; Stassun et al. 2012) and strong coronal X-ray emission (López-Morales 2007; Feiden & Chaboyer 2012a). Both are thought to be indicative of magnetic fields heating the stellar atmosphere. Magnetic activity levels may also correlate with radius inflation (López-Morales 2007; Stassun et al. 2012), but it is still an open question (Feiden & Chaboyer 2012a). Such a correlation would be strong evidence implicating magnetic fields as the culprit of radius inflation.

Indirect measures of magnetic field strengths (i.e., magnetic activity indicators) yield tantalizing clues about the origin of the observed radius inflation, but direct measurements are far more preferable. Although no direct observations of surface magnetic fields on low-mass DEBs have been published,[3] there has been a concerted effort to measure surface magnetic field strengths of single low-mass stars (e.g., Saar 1996; Reiners & Basri 2007, 2009; Johns-Krull 2007; Morin et al. 2010; Shulyak et al. 2011; Reiners 2012). K- and M-dwarfs have been a focus of magnetic field studies because around mid-M spectral type, about 0.35 $M_{\odot}$, M-dwarfs become fully convective (Limber 1958; Baraffe et al. 1998). Standard descriptions of the stellar dynamo mechanism posit that magnetic fields are generated near the base of the outer convection zone (Parker 1955, 1979). A strong shear layer, called the tachocline, forms between the differentially rotating convection zone and the radiation zone, which rotates as a solid body. Fully convective stars, by definition, do not possess a tachocline. Thus, according to the standard Parker dynamo model, this would leave fully convective stars unable to generate or sustain a strong magnetic field.

Despite lacking a tachocline, low-mass stars are observed to possess strong magnetic fields with surface strengths upward of a few kilogauss (Saar 1996; Reiners & Basri 2007, 2010; Reiners et al. 2009; Shulyak et al. 2011). Instead of a dynamo primarily powered by rotation, turbulent convection may be driving the stellar dynamo (Durney et al. 1993; Dobler et al. 2006; Chabrier & Küker 2006). Large-scale magnetic field topologies of low-mass stars appear to shift from primarily non-axisymmetric to axisymmetric across the fully convective boundary (Morin et al. 2008, 2010; Donati & Landstreet 2009; Phan-Bao et al. 2009). This apparent shift in field topology is suggested as the hallmark of a transitioning dynamo. However, shifts in field topology are still a subject for debate (Donati & Landstreet 2009; Reiners 2012). It is also uncertain whether the transition from a rotational

[3] Morin et al. (2013) report the observations, but not the results, of such an endeavor.

Table 1
Sample of DEBs Whose Stars Possess a Radiative Core

DEB System	Star	P_{orb} (day)	Mass ($M_\odot$)	Radius ($R_\odot$)	T_{eff} (K)	[Fe/H] (dex)
UV Psc	A	0.86	0.9829 ± 0.0077	1.110 ± 0.023	5780 ± 100	...
UV Psc	B		0.76440 ± 0.00450	0.8350 ± 0.0180	4750 ± 80	...
YY Gem	A	0.81	0.59920 ± 0.00470	0.6194 ± 0.0057	3820 ± 100	$+0.1 \pm 0.2$
YY Gem	B		0.59920 ± 0.00470	0.6194 ± 0.0057	3820 ± 100	$+0.1 \pm 0.2$
CU Cnc	A	2.77	0.43490 ± 0.00120	0.4323 ± 0.0055	3160 ± 150	...
CU Cnc	B		0.39922 ± 0.00089	0.3916 ± 0.0094	3125 ± 150	...

to a turbulent dynamo occurs abruptly at the fully convective boundary or if it is a gradual transition developing between early- and mid-M-dwarfs.

With the dynamo dichotomy in mind, we have elected to divide our analysis of the low-mass stellar mass-radius problem into two parts. The first part, presented in this paper, concerns low-mass stars in DEBs that should possess a radiative core and convective outer envelope. The second part, pertaining to fully convective low-mass stars, is presented in a companion paper (G. A. Feiden & B. Chaboyer, in preparation). Our motivation for splitting the analysis is that models described in Feiden & Chaboyer (2012b) assume that energy for the magnetic field—and thus the dynamo mechanism—is supplied by rotation. This was explicitly stated following the discussion of Equation (41) in that paper. With the onset of complete convection near $M = 0.35\,M_\odot$, a transition from a rotationally driven interface dynamo to a turbulent dynamo must occur. Thus, the theory that we present in Feiden & Chaboyer (2012b) is probably not suitable for models of fully convective stars. Whether our theory is valid for partially convective stars is an answer that will be pursued in this work.

We present results from detailed modeling of three DEB systems with partially convective stars. We study only three systems to avoid muddling the results while still providing a rigorous examination of the models. The three DEBs selected for analysis were UV Piscium (Carr 1967; Popper 1997), YY Geminorum (Adams & Joy 1920; Torres & Ribas 2002), and CU Cancri (Delfosse et al. 1999; Ribas 2003). We recall their properties in Table 1.

These three particular systems were chosen for three reasons: (1) they are well studied, meaning they have precisely determined masses and radii with reasonable estimates of their effective temperatures, (2) they show large discrepancies with models (Feiden & Chaboyer 2012a), and (3) they span an interesting range in mass, covering nearly the full range of masses for partially convective low-mass stars. This latter fact will allow us to assess the validity of our modeling assumptions as we approach the fully convective boundary. Effectively, we will probe whether an interface dynamo of the type presented by Parker (1955) is sufficient to drive the observed inflation, or if a turbulent dynamo is required to deplete the kinetic energy available in convective flows.

The paper is organized as follows: a discussion of the adopted stellar models is presented in Section 2. In Section 3, we demonstrate that our models are able to reconcile the observed radius and T_{eff} discrepancies. Discussion presented in Section 4, however, leads us to believe that magnetic field strengths required by our models are unrealistic. We therefore explore various means of reducing the surface magnetic field strengths. A further discussion of our results is given in Section 5. We provide comparisons of different models and to previous studies. Implications for asteroseismology studies and exoplanet investigations are also considered. Finally, we summarize the key conclusions in Section 6.

2. DARTMOUTH MAGNETIC STELLAR EVOLUTION CODE

Stellar evolution models were computed as a part of the Dartmouth Magnetic Evolutionary Stellar Tracks and Relations program (Feiden & Chaboyer 2012b; Feiden 2013). The stellar evolution code is a modified version of the existing Dartmouth stellar evolution code (Dotter et al. 2008). Physics used by the standard (i.e., non-magnetic) Dartmouth code have been described extensively in the literature (e.g., Dotter et al. 2007, 2008; Feiden et al. 2011; Feiden & Chaboyer 2012a, 2012b) and will not be reviewed here. We note that we have updated the nuclear reaction cross sections to those recommended by Adelberger et al. (2011). The latest recommendations include a revised cross section for the primary channel of the proton–proton (p–p) chain, but it does not significantly impact low-mass stellar evolution.

Effects of a globally pervasive magnetic field are included following the prescription described by Feiden & Chaboyer (2012b), which is heavily based on the procedure outlined by Lydon & Sofia (1995). Perturbations to the canonical stellar structure equations are treated self-consistently by considering thermodynamic consequences of stresses associated with a static magnetic field. Modifications to the standard convective mixing length theory (MLT; e.g., Böhm-Vitense 1958) are derived self-consistently by assuming the magnetic field is in thermodynamic equilibrium with the surrounding plasma. All transient magnetic phenomena that act to remove mass, such as flares and coronal mass ejections, are ignored. We also neglect the steady removal of mass through magnetized stellar winds. There does not appear to be significant mass loss from low-mass stars (Laughlin et al. 1997 and references therein).

Input variables for stellar evolution models are defined relative to calibrated solar values. These input variables include the stellar mass, the initial mass fractions of helium and heavy elements (Y_i and Z_i, respectively), and the convective mixing length parameter, α_{MLT}. The latter defines the length scale of a turbulent convective eddy in units of pressure scale heights. Since they are all defined relative to the solar values, we must first define what constitutes the Sun for the model setup. To do this, we require a $1.0\,M_\odot$ model to reproduce the solar radius, luminosity, radius to the base of the convection zone, and the solar photospheric (Z/X) at the solar age (4.57 Gyr; Bahcall et al. 2005). Adopting the solar heavy element abundance of Grevesse & Sauval (1998), our models require $Y_{init} = 0.27491$, $Z_{init} = 0.01884$, and $\alpha_{MLT} = 1.938$. The final solar model properties are given in Table 2.

Table 2
Solar Calibration Properties

Property	Adopted	Model	Reference
Age (Gyr)	4.57	...	1
$M_\odot$ (g)	1.9891×10^{33}	...	2
$R_\odot$ (cm)	6.9598×10^{10}	$\log(R/R_\odot) = 8 \times 10^{-5}$	3, 1
$L_\odot$ (erg s^{-1})	3.8418×10^{33}	$\log(L/L_\odot) = 2 \times 10^{-4}$	1
$R_{\rm bcz}/R_\odot$	0.713 ± 0.001	0.714	4, 5
$(Z/X)_{\rm surf}$	0.0231	0.0230	6
$Y_{\odot,\,\rm surf}$	0.2485 ± 0.0034	0.2455	7

References. (1) Bahcall et al. 2005; (2) IAU 2009 (3) Neckel 1995; (4) Basu & Antia 1997; (5) Basu 1998; (6) Grevesse & Sauval 1998; (7) Basu & Antia 2004.

3. ANALYSIS OF INDIVIDUAL DEB SYSTEMS

3.1. UV Piscium

UV Piscium (HD 7700; hereafter UV Psc) contains a solar-type primary with a mid-K-dwarf companion. Numerous determinations the fundamental stellar properties have been performed since its discovery, with the most precise measurements produced by Popper (1997). These measurements were later slightly revised by Torres et al. (2010), who standardized reduction and parameter extraction routines for a host of DEB systems. The mass and radius for each component of UV Psc recommended by Torres et al. (2010) is given in Table 1. No metallicity estimate exists, despite the system being relatively bright ($V = 9.01$) and having a nearly total secondary eclipse.

One notable feature of UV Psc is that the secondary component is unable to be properly fit by standard stellar evolution models at the same age as the primary (see, e.g., Popper 1997; Lastennet et al. 2003; Torres et al. 2010; Feiden & Chaboyer 2012a). The secondary's radius appears to be approximately 10% larger than models predict and the effective temperature is about 6% cooler than predicted. Metallicity and age are known to affect the stellar properties predicted by models, typically allowing for better agreement with observations. However, even when allowing for age and metallicity variation, the best fit models of UV Psc display large disagreements (Feiden & Chaboyer 2012a).

An investigation by Lastennet et al. (2003) found that it was possible to fit the components on the same theoretical isochrone. Their method involved independently adjusting the helium mass fraction Y, the metal abundance Z, and the convective mixing length $\alpha_{\rm MLT}$. The authors were able to constrain a range of Y, Z, and $\alpha_{\rm MLT}$ values that produced stellar models compatible with the fundamental properties of each component while enforcing that the stars be coeval. Lastennet et al. (2003) found that a sub-solar metal abundance ($Z = 0.012$)[4] combined with an enhanced helium abundance ($Y = 0.31$) and drastically reduced mixing lengths for each star produced the best fit at an age of 1.9 Gyr. The final mixing lengths were $\alpha_{\rm MLT} = 0.58\alpha_{\rm MLT,\,\odot}$ and $0.40\alpha_{\rm MLT,\,\odot}$, for the primary and secondary, respectively, where $\alpha_{\rm MLT,\,\odot}$ is the solar calibrated mixing length. The age inferred from their models is a factor of four lower than the 8 Gyr age commonly cited for the system.

Despite properly fitting the two components, the investigation by Lastennet et al. (2003) did not provide any physical justification for the reduction in mixing length. Furthermore, they required an abnormally high helium abundance given the required sub-solar heavy element abundance. Assuming that Y varies linearly with Z according to the formula

$$Y = Y_p + \left(\frac{\Delta Y}{\Delta Z}\right)(Z - Z_p), \quad (1)$$

where Y_p is the primordial helium mass fraction and Z_p is the primordial heavy element abundance ($Z_p = 0$), implies that $\Delta Y/\Delta Z > 5$ for the Lastennet et al. (2003) study. Empirically determined values typically converge around 2 ± 1 (Casagrande et al. 2007). The empirical relation is by no means certain and there is no guarantee that all stars conform to this prescription. However, a single data point suggesting $\Delta Y/\Delta Z > 5$ is a significant outlier, at 3σ above the empirical relation. This introduces some doubt as to whether that particular Y and Z combination is realistic. Though we cannot definitively rule out the results of the Lastennet et al. (2003) study, we seek an alternative explanation to reconcile the stellar models with observations of the secondary.

The stars in UV Psc exhibit strong magnetic activity, showcasing a wide variety of phenomena. Soft X-ray emission (Agrawal et al. 1980), Ca II H & K emission (Popper 1976; Montes et al. 1995a), and Hα emission (Barden 1985; Montes et al. 1995b) have all been observed and associated with UV Psc. Flares have been recorded in Hα (Liu et al. 1996) and at X-ray wavelengths (Caillault 1982), further suggesting the components are strongly active. Star spots betray their presence in the modulation and asymmetries of several light curves (Kjurkchieva et al. 2005). Although some of these modulations have also been attributed to intrinsic variability in one of the components (Antonopoulou 1987), there does not appear to be any further evidence supporting this claim (Ibanoglu 1987; Popper 1997). This leads us to believe any observed light curve variations are the result of spots.

The aforementioned evidence provides clues that magnetic fields may be the source of the observed radius discrepancies. Lastennet et al.'s (2003) finding that a reduced convective mixing length was required could then be explained by magnetic inhibition of thermal convection (Cox et al. 1981; Chabrier et al. 2007).

Previous studies of UV Psc have found that standard stellar evolution models are able to reproduce the fundamental stellar properties of the primary star (Popper 1997; Lastennet et al. 2003; Torres et al. 2010; Feiden & Chaboyer 2012a). Therefore, we begin by assuming that UV Psc A conforms to the predictions of stellar evolution theory, but that magnetic effects must be invoked to reconcile models with UV Psc B. Given this assumption, UV Psc A may be used to constrain the age and metallicity of the system. Using a large grid of stellar evolution isochrones, Feiden & Chaboyer (2012a) found UV Psc A was best fit by a 7 Gyr isochrone with a slightly metal-poor composition of -0.1 dex. The metallicity estimate is consistent with Lastennet et al. (2003), though two independent methods were utilized to achieve the result. We adopt this sub-solar value as the initial target age and metallicity for the system.

Standard model mass tracks are illustrated in Figures 1(a) and (b) for two different metallicities. The age of the system is anchored to the narrow region in Figure 1(a) where the models agree with the observed primary radius. Figure 1(b) indicates that the [Fe/H] $= -0.1$ model yields satisfactory agreement with the observed radius and effective temperature. We infer an age of 7.2 Gyr, which is more precise than Feiden &

[4] We calculate this implies [Fe/H] $= -0.14$ considering the required Y and the fact that they were using the Grevesse & Noels (1993) heavy element abundances.

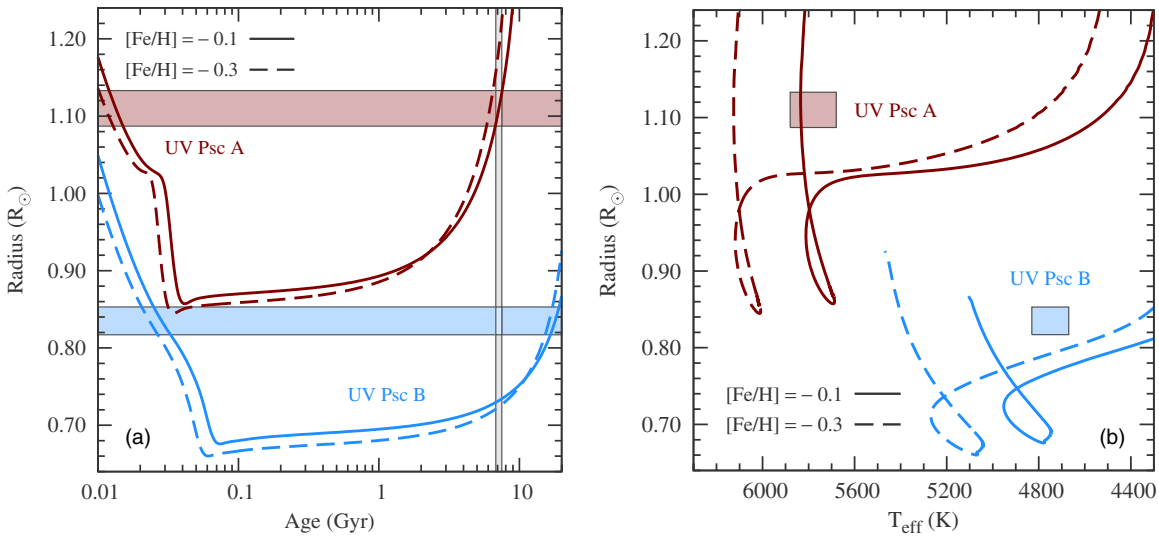

Figure 1. Standard Dartmouth mass tracks of UV Psc A (maroon) and UV Psc B (light blue) computed with [Fe/H] = −0.1 (solid line) and [Fe/H] = −0.3 (dashed line). (a) The age–radius plane. Horizontal swaths denote the observed radii with associated 1σ uncertainty. The vertical region indicates the age predicted by the primary. (b) The $T_{\rm eff}$–radius plane. Shaded regions denote the observational constraints.

(A color version of this figure is available in the online journal.)

Chaboyer (2012a) as we are not constrained to a discretized set of isochrone ages. Standard models for the secondary are shown to reach the observed radius at an age of 18 Gyr, according to Figure 1(a). This implies an 11 Gyr difference between the two components. We also see that the model effective temperature of the secondary is too hot compared to observations by about 250 K.

Magnetic models of the secondary component were computed using a dipole profile, single-step perturbation at 10 Myr for several values of the surface magnetic field strength. A surface magnetic field strength of 4.0 kG (corresponding to a tachocline field strength of 11 kG) produced a model radius that was in agreement with the observed radius at 7.2 Gyr. This is depicted in Figure 2(a). The dashed line, representing the magnetic model of the secondary, passes through the narrow region formed by the intersection of the radius (horizontal shaded area) and age (vertical shaded area) constraints.

We checked that the effective temperature predicted by the magnetic model agreed with the temperature inferred from observations. Figure 2(b) shows the same 4.0 kG magnetic mass track required to fit the secondary in the age–radius plane over-suppresses the effective temperature. This causes the model to be too cool compared to the empirical value. Intuitively, one might suggest lowering the surface magnetic field strength so as to maintain agreement in the age–radius plane while allowing for a hotter effective temperature. However, all values of the surface magnetic field strength that provide agreement in the age–radius plane produce models that are cooler than the empirical temperature.

How might we interpret the remaining temperature disagreement? One possible solution is that the effective temperature measurement is incorrect. We feel this scenario is unlikely considering the temperatures are hot enough where large uncertainties associated with complex molecular bands are not present. The uncertainties quoted in Table 1 seem large enough to encompass the actual value. Another possibility is that we have not treated convection properly. Convection within the component stars may not have the same inherent properties as convection within the Sun. This idea has continually motivated modelers to freely adjust the convective mixing length. However, while MLT is not entirely realistic and allows for such an arbitrary choice of the mixing length, arbitrary reduction without a definite physical motivation (other than providing better empirical agreement) is not wholly satisfying. Glossing over the specific reasons for mixing length reduction does not fully illuminate the reasons for the noted discrepancies.

Instead of applying an arbitrary adjustment to the convective mixing length, we modify the convective mixing length parameter according to the relation developed by Bonaca et al. (2012). Using asteroseismic data, they provide a relation between the mixing length parameter and stellar physical properties (i.e., $\log g$, $T_{\rm eff}$, and [M/H]). Their formulation indicates that convection is less efficient (smaller mixing length) in low-mass, metal-poor stars as compared to the solar case. Modifications to the convective mixing length are, therefore, no longer arbitrary and may not take on any value that happens to allow the models to fit a particular case.

The Bonaca et al. (2012) relation is based on models using an Eddington $T(\tau)$ relation to derive the surface boundary conditions, meaning they require a solar calibrated mixing length of 1.69. Our use of PHOENIX model atmosphere structures to derive the surface boundary conditions and treatment of atomic diffusion of helium leads to our higher solar calibrated mixing length of $\alpha_{\rm MLT,\odot} = 1.94$. We therefore use the Bonaca et al. (2012) relation to derive the relative difference between the empirically derived mixing length and their solar calibrated value, keeping their fit coefficients fixed. New mixing lengths for the stars in UV Psc are scaled from our solar mixing length using this relative difference. For a metallicity of −0.1 dex, we find a mixing length of $\alpha_{\rm MLT} = 1.71$ for the primary and $\alpha_{\rm MLT} = 1.49$ for the secondary of UV Psc.

Resulting mass tracks are shown in Figure 3. Directly altering convection in this manner does not provide an adequate solution. Reducing the mixing length inflates both of the stellar radii (Figure 3(a)) and forces the temperature at the photosphere to decrease (see Figure 3(b)). The mixing length primarily affects the outer layers of each star, where energy is transported by super-adiabatic convection. A lower mixing length implies

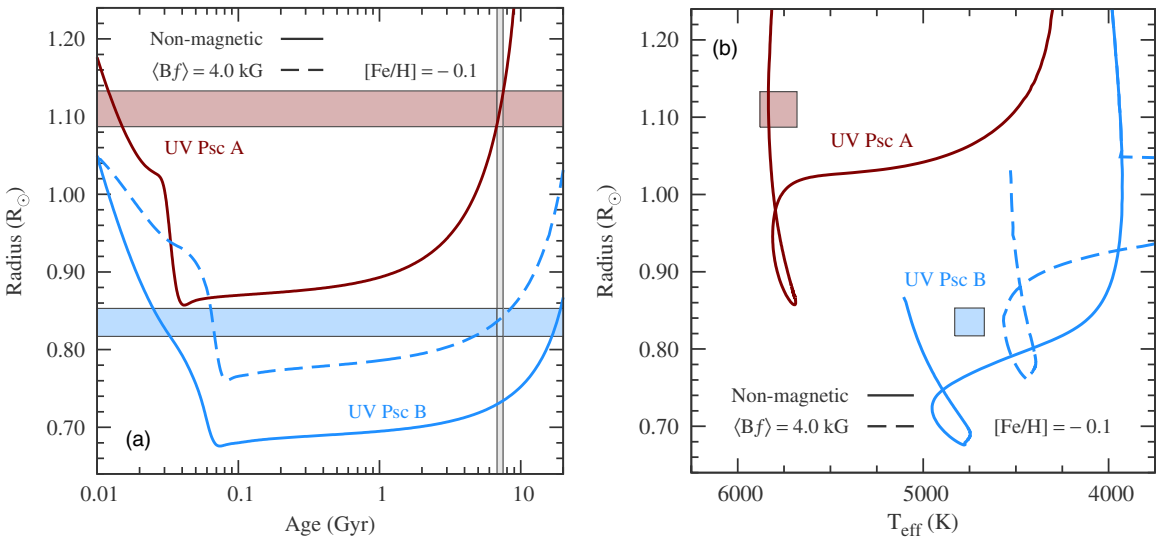

Figure 2. Similar to Figure 1 but with a single metallicity of [Fe/H] = −0.1 dex. Magnetic mass track for UV Psc B with a 4.0 kG surface magnetic field strength (light blue, dashed line). Standard Dartmouth mass tracks are plotted for comparison. (a) Age–radius plane. (b) $T_{\rm eff}$–radius plane.

(A color version of this figure is available in the online journal.)

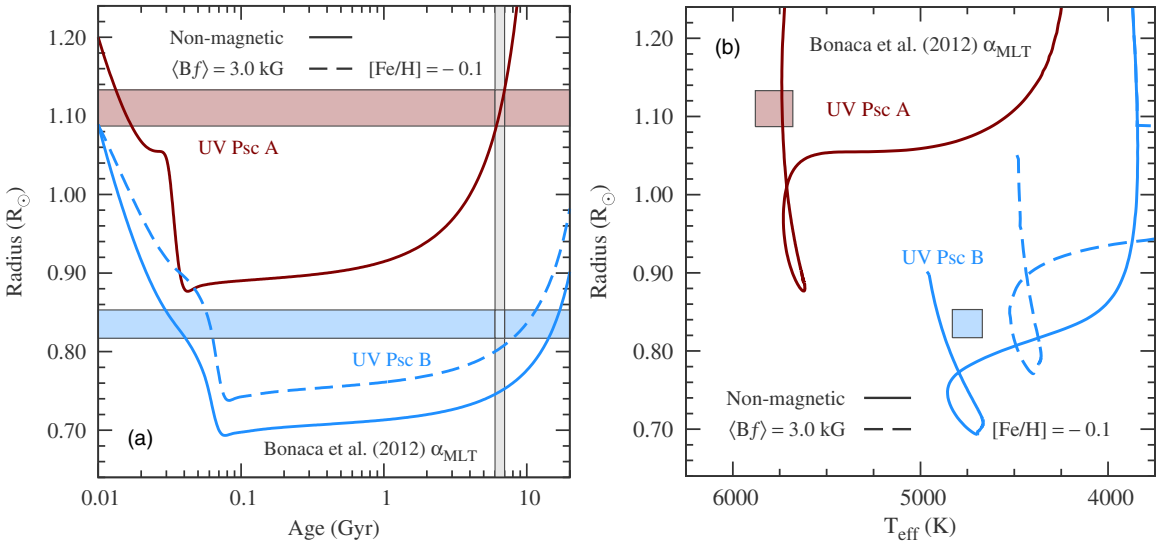

Figure 3. Similar to Figure 2 except that all of the mass tracks have a $\alpha_{\rm MLT}$ reduced according to the Bonaca et al. (2012) empirical relation. The surface magnetic field strength used in modeling the secondary is 3.0 kG. (a) Age–radius plane. (b) $T_{\rm eff}$–radius plane.

(A color version of this figure is available in the online journal.)

that there is less energy flux across a given surface within the convection zone. Since the star must remain in equilibrium, the outer layers puff up to increase the energy flux, thereby reducing the effective temperature.

Inflating the primary component means the models of the secondary must now agree with the observed properties at an age younger than 7.2 Gyr. This is illustrated in Figure 3(a), where the vertical shaded area anchoring the system's age to UV Psc A is shifted left of where it was in Figure 1(a) by 0.5 Gyr. A weaker magnetic field is now required to alleviate the radius disagreement with the secondary due to inflation caused by a reduced mixing length. Figure 3(a) shows a magnetic model with a surface magnetic field strength of 3.0 kG. We do not find agreement between the model and empirical radius, but more importantly, Figure 3(b) demonstrates that the secondary's effective temperature is too cool. Increasing the surface magnetic field strength to produce agreement in the age–radius plane would only worsen the lack of agreement in the $T_{\rm eff}$–radius plane. Thus, reducing the mixing length is unable to provide relief to the magnetic over-suppression of the effective temperature in Figure 2(b). We must seek another method to rectify the effective temperature of the magnetic model.

Metallicity is an unconstrained input parameter for models of UV Psc. Recall, our selection of [Fe/H] = −0.1 was motivated by agreement of standard stellar evolution models with the primary. Updating our adopted metallicity (and consequently, the helium abundance) has a non-negligible effect the structure and evolution of the UV Psc components. Stars with masses above ∼0.45 $M_{\odot}$ are similarly affected by altering the chemical composition. For example, increasing the metallicity, and therefore the helium abundance, will increase the stellar radii and decrease the effective temperature. This is a result of changes to the p–p chain energy generation rate due to helium and the influence of both helium and heavy metals on bound-free radiative opacity.

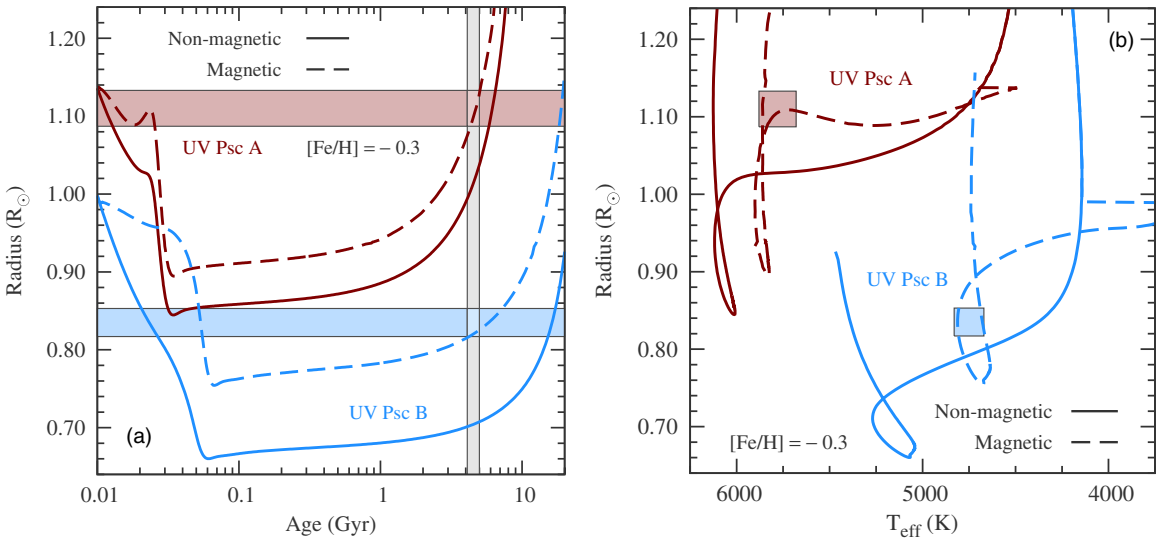

Figure 4. UV Psc system assuming a lower heavy element abundance of [Fe/H] = −0.3. Standard DSEP mass tracks are drawn as maroon and light blue solid lines for UV Psc A and B, respectively. Magnetic tracks are represented by dashed lines with the same color coding as the standard tracks. Surface magnetic field strengths are 2.0 kG and 4.6 kG for UV Psc A and B, respectively. (a) Age–radius plane. (b) $T_{\rm eff}$–radius plane.

(A color version of this figure is available in the online journal.)

Adopting a lower metallicity of [Fe/H] = −0.3, while maintaining a solar calibrated $\alpha_{\rm MLT}$ = 1.94, for UV Psc increases the effective temperature of both standard model components and shrinks their radii at younger ages.[5] Doing so also removes the effective temperature agreement between models and observations of UV Psc A. These effects are demonstrated for standard models in Figures 1(a) and (b), where we have plotted mass tracks with [Fe/H] = −0.3. Accurately reproducing the observed stellar properties now requires use of magnetic models for *both* components.

Magnetic models with a dipole profile and single-step perturbation were constructed for both stars. We find that it is possible to wholly reconcile the models with the observations if the primary has a 2.0 kG surface magnetic field and the secondary has a 4.6 kG surface magnetic field. Model radii and temperatures match the empirical values within the age range specified by the primary, as shown in Figures 4(a) and (b).

The revised age of UV Psc found from Figure 4(a) (the vertical shaded region) is between 4.4 Gyr and 5.0 Gyr. Averaging the two implies an age of 4.7 ± 0.3 Gyr. This age is nearly a factor of two younger than the 7 Gyr–8 Gyr age commonly prescribed to the system. While feedback from the models was necessary to adjust and improve upon the initial metallicity and to determine the required magnetic field strengths, we believe that this result is consistent with the available observational data. Our reliance on such a feedback cycle was inevitable given the lack of metallicity estimates. The metallicity range allowing for complete agreement is not limited to −0.3 dex. Further reducing the metallicity would likely produce acceptable results, as the models of UV Psc B just barely skirt the boundaries of the empirical values. Our final recommendation is that UV Psc has a metallicity of [Fe/H] = −0.3 ± 0.1 dex with surface magnetic fields of 2.0 kG and 4.6 kG for the primary and secondary, respectively. Verification of these predictions should be obtainable using spectroscopic methods.

[5] At older ages, evolutionary effects begin to play a role as stellar lifetimes are decreased at lower metallicity owing to higher temperatures within the stellar interior.

3.2. YY Geminorum

YY Geminorum (also Castor C and GJ 278 CD; hereafter YY Gem) has been the subject of extensive investigation after hints of its binary nature were spectroscopically uncovered (Adams & Joy 1920). The first definitive reports of the orbit were published nearly simultaneously using spectroscopic (Joy & Sanford 1926) and photographic methods (van Gent 1926), which revealed the system to have an incredibly short period of 0.814 days. Photographic study by van Gent (1926) further revealed that the components eclipsed one another with the primary and secondary eclipse depths appearing nearly equal. Rough estimates of the component masses and radii were carried out using the available data, but the data were not of sufficient quality to extract reliable values (Joy & Sanford 1926). The system has since been confirmed to consist of two equal mass, early M-dwarfs. Masses and radii are now established with a precision of under 1% (Torres & Ribas 2002). These measurements are presented in Table 1.

The age and metallicity of YY Gem have been estimated using YY Gem's common proper motion companions, Castor A and B. Considered gravitationally bound, these three systems have been used to define the Castor moving group (CMG; Anosova et al. 1989). Spectroscopy of Castor Aa and Ba, both spectral-type A stars, yields a metallicity of [Fe/H] = +0.1 ± 0.2 (Smith 1974; Torres & Ribas 2002). Stellar evolution models of Castor Aa and Castor Ba provide an age estimate of 359 ± 34 Myr, which was obtained by combining estimates from multiple stellar evolution codes (Torres & Ribas 2002), including the Dartmouth code (Feiden & Chaboyer 2012a).

Over half a century after its binarity was uncovered, low-mass stellar evolution models suggested that the theoretically predicted radii may not agree with observations (Hoxie 1970, 1973). A subsequent generation of models appeared to find agreement with the observations (Chabrier & Baraffe 1995), but confirmation of the true discrepancies remained veiled by model and observational uncertainties. Modern observational determinations of the stellar properties (Ségransan et al. 2000; Torres & Ribas 2002) compared against sophisticated low-mass stellar evolution models (Baraffe et al. 1998; Dotter et al. 2008)

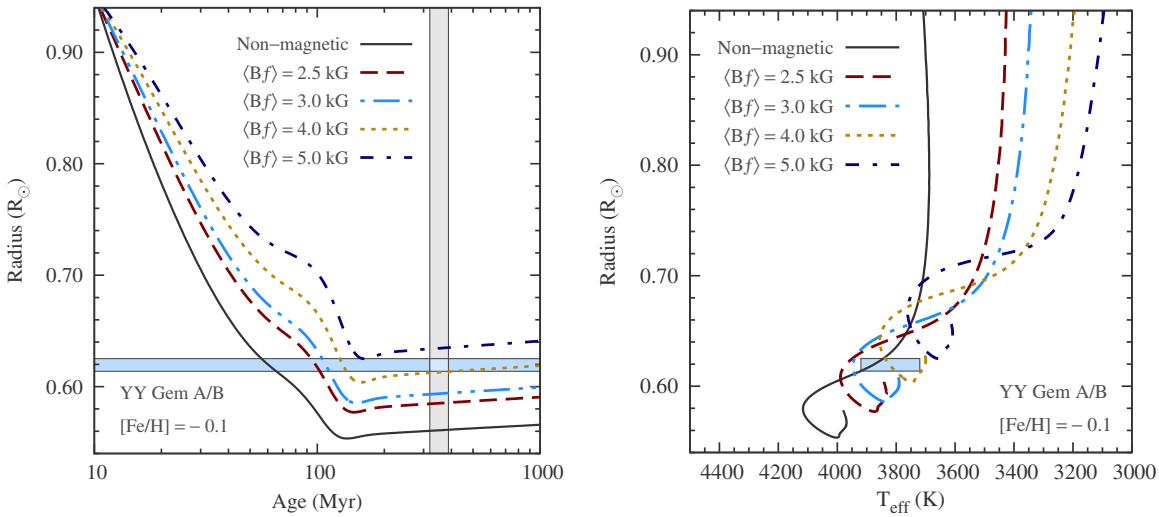

Figure 5. Standard (dark gray, solid line) and magnetic stellar evolution mass tracks of YY Gem. Magnetic mass tracks were generated with surface magnetic field strengths of $\langle Bf \rangle = 2.5$ kG (maroon, dashed), 3.0 kG (light blue, dash-double-dotted), 4.0 kG (mustard, dotted), and 5.0 kG (dark blue, dash-dotted). All of the models were computed with a metallicity [Fe/H] $= -0.1$. Shown are the (a) age–radius plane, and (b) $T_{\rm eff}$–radius plane. The horizontal swaths represent the observational constraints in each plane while the vertical shaded region in panel (a) shows the estimated age constraints set by modeling of Castor A and B.

(A color version of this figure is available in the online journal.)

have now solidified that the components of YY Gem appear inflated by approximately 8% (Torres & Ribas 2002; Feiden & Chaboyer 2012a).

Figure 5 shows a standard stellar evolution mass track for the components of YY Gem as a dark gray, solid line. We plot an $M = 0.599\,M_{\odot}$ mass with a metallicity of [Fe/H] $= -0.1$. That metallicity was found to provide good agreement to observational data by Feiden & Chaboyer (2012a). The vertical shaded region highlights YY Gem's adopted age. Figure 5(a) indicates that the standard model under predicts the radius measured by Torres & Ribas (2002) (illustrated by the horizontal shaded region) by about 8%, within the required age range. Similarly, there is a 5% discrepancy with the effective temperature shown in Figure 5(b).

As a brief aside, it may be noted from Figure 5(a) that our models are consistent with the properties of YY Gem around 60 Myr. This age would imply that YY Gem has not yet settled onto the MS, which occurs near an age of about 110 Myr. Previous studies have considered the possibility that YY Gem is still undergoing its pre-MS contraction (Chabrier & Baraffe 1995; Torres & Ribas 2002) and provide mixed conclusions. However, the more recent study by Torres & Ribas (2002) provides a detailed analysis of this consideration and concludes that it is erroneous to assume YY Gem is a pre-MS system. This is primarily due to YY Gem's association with the Castor quadruple. YY Gem is considered to be firmly on the MS, making the system discrepant with stellar models.

YY Gem exhibits numerous features indicative of intense magnetic activity. Light curve modulation has been continually observed (Kron 1952; Leung & Schneider 1978; Torres & Ribas 2002), suggesting the presence of star spots. Debates linger about the precise latitudinal location and distribution (e.g., Güdel et al. 2001) of star spots, but spots contained below mid-latitude (between 45° and 50°) appear to be favored (Güdel et al. 2001; Hussain et al. 2012). The components display strong Balmer emission (Young et al. 1989; Montes et al. 1995b) and X-ray emission (Güdel et al. 2001; Stelzer et al. 2002; López-Morales 2007; Hussain et al. 2012) during quiescence and have been observed to undergo frequent flaring events (Doyle et al. 1990; Doyle & Mathioudakis 1990; Hussain et al. 2012). Furthermore, YY Gem has been identified as a source of radio emission, attributed to partially relativistic electron gyrosynchrotron radiation (Güdel et al. 1993; McLean et al. 2012). Given this evidence, it is widely appreciated that the stars possess strong magnetic fields. Therefore, it is plausible to hypothesize that the interplay between convection and magnetic fields lies at the origin of the model-observation disagreements.

We compute magnetic stellar evolution mass tracks with various surface magnetic field strengths. The magnetic perturbation was included using a dipole magnetic field configuration and was added in a single time step. These tracks are plotted in Figures 5(a) and (b). We adopt a metallicity of −0.1 dex, consistent with our non-magnetic model. The level of radius inflation and temperature suppression increases as progressively stronger values of the surface magnetic field strength are applied. A 5.0 kG surface magnetic field strength model over predicts the observed stellar radii. Figure 5(a) demonstrates that a surface magnetic field strength of just over 4.0 kG is needed to reproduce the observed radii.

Figure 5(b) reveals that the models are barely able to match the observed effective temperature with a 4.0 kG magnetic field. Any stronger of a surface magnetic field over-suppresses the effective temperature, causing the model to be cooler than the observations. Recall, we encountered this same issue when attempting to model UV Psc in Section 3.1. A lower metallicity provides a solution for UV Psc, but doing so for YY Gem would jeopardize the metallicity prior established by the association with Castor AB (Smith 1974; Torres & Ribas 2002).

Before ruling out the option of a lower metallicity, we recompute the approximate metallicity of YY Gem using the Smith (1974) values. First, we need to determine the metallicity of Vega, the reference for the Smith (1974) study. Vega has 21 listed metallicity measurements in SIMBAD, of which, the 8 most recent appear to be converge toward a common value. Using the entire list of 21 measurements, Vega has a metallicity of [Fe/H] $= -0.4 \pm 0.4$ dex. If, instead, we adopt only those measurements performed since 1980, we find [Fe/H] $= -0.6 \pm 0.1$ dex. The convergence of values in

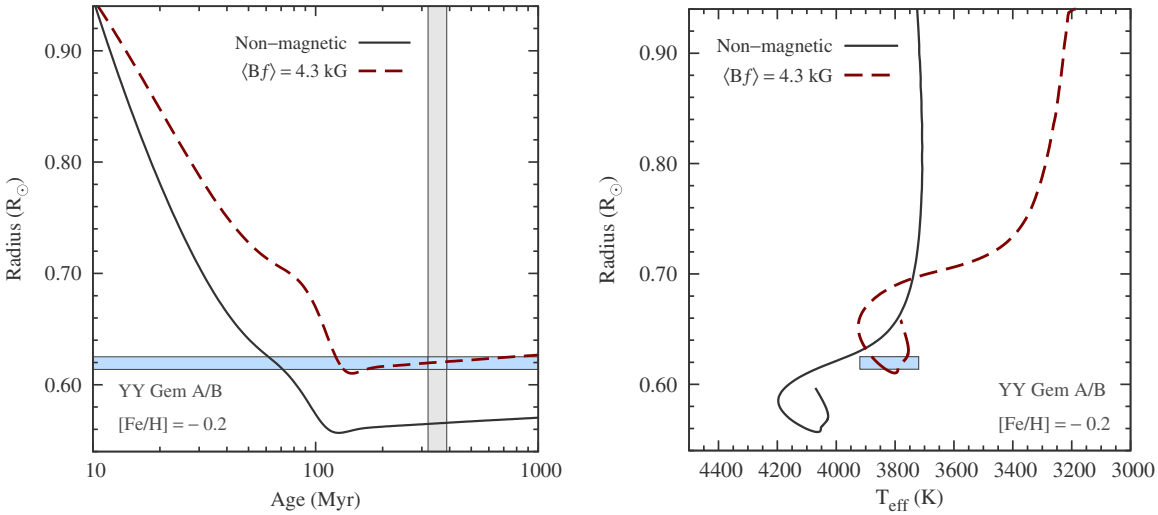

Figure 6. Standard (dark gray, solid line) and magnetic stellar evolution mass tracks of YY Gem. The magnetic mass track was generated with a surface magnetic field strength of $\langle Bf \rangle = 4.3$ kG (maroon, dashed). Both of the models were computed with a metallicity [Fe/H] $= -0.2$. Shown are the (a) age–radius plane, and (b) $T_{\rm eff}$–radius plane. The horizontal swaths represent the observational constraints in each plane while the vertical shaded region in panel (a) shows the estimated age constraints set by modeling of Castor A and B.

(A color version of this figure is available in the online journal.)

recent years leads us to believe that this latter estimate is more representative of Vega's metallicity.

Metallicities measured by Smith (1974) for Castor A and Castor B were +0.98 dex and +0.45 dex, respectively. Averaging these two quantities as the metallicity for the Castor AB system, we have [Fe/H] $= +0.7 \pm 0.3$ dex. The difference in metallicity of Castor A and B might be explained by diffusion processes (e.g., Richer et al. 2000) and is not necessarily a concern. However, the fact that we are not observing the initial abundances for Castor A and B is a concern when it comes to prescribing a metallicity for YY Gem. Caution aside, a conservative estimate for the metallicity of YY Gem relative to the Sun is [Fe/H] $= +0.1 \pm 0.4$ dex. This new estimate provides greater freedom in our model assessment of YY Gem. We note that this reassessment neglects internal errors associated with the abundance determination performed by Smith (1974). Given the large uncertainty quoted above, the real metallicity is presumed to lie within the statistical error. Confirmation of these abundances would be extremely beneficial. New abundance determinations would not only enhance our understanding of YY Gem, but also provide evidence that the three binaries comprising the Castor system have a common origin.

Presented with greater freedom in modeling YY Gem, we compute additional standard and magnetic mass tracks with [Fe/H] $= -0.2$ dex. The magnetic tracks were computed in the same fashion as the previous set to provide a direct comparison on the effect of metallicity. Figures 6(a) and (b) illustrate the results of these models. Reducing the metallicity from [Fe/H] $= -0.1$ to [Fe/H] $= -0.2$ dex shrinks the standard model radius by about 1% at a given age along the MS. As anticipated, a standard model with a revised metallicity also shows a 50 K hotter effective temperature.

A magnetic mass track with a surface magnetic field of 4.3 kG was found to provide good agreement. At 360 Myr, it is apparent that the magnetic model of YY Gem satisfies the radius restrictions enforced by the observations. The precise model radius inferred from the mass track is 0.620 $R_\odot$, compared to the observed radius of 0.6194 $R_\odot$, a difference of 0.1%. Figure 6(b) further demonstrates that when the model is consistent with the observed radius, the effective temperature of the mass track is in agreement with the observations. The model effective temperature at 360 Myr is 3773 K, well within the 1σ observational uncertainty (also see Table 1).

There is one additional constraint that we have yet to mention. Lithium has been detected in the stars of YY Gem (Barrado y Navascués et al. 1997). The authors find $\log N(^7\mathrm{Li}) = 0.11$, where $\log N(^7\mathrm{Li}) = 12 + \log(X_{\rm Li}/A_{\rm Li}X_{\rm H})$. However, standard stellar models predict that lithium is completely depleted from the surface after about 15 Myr—well before the stars reach the MS. Since magnetic fields can shrink the surface convection zone, it is possible for the fields to extend the lithium depletion timescale (MacDonald & Mullan 2010). This is precisely what our magnetic models predict. With a metallicity of [Fe/H] $= -0.2$ and a 4.3 kG surface magnetic field our models predict $\log N(^7\mathrm{Li}) \sim 0.9$ at 360 Myr. With [Fe/H] $= -0.1$ and a 4.0 kG we find $\log N(^7\mathrm{Li}) = 0.1$ at 360 Myr. The latter value is consistent with the lithium abundance determination of Barrado y Navascués et al. (1997), but is inconsistent with the metallicity motivated by agreement with the fundamental stellar properties.

In summary, we find good agreement with magnetic models that have a surface magnetic field strength between 4.0 and 4.5 kG. A sub-solar metallicity of [Fe/H] $= -0.2$ provides the most robust fit with fundamental properties, but a metallicity as high as [Fe/H] $= -0.1$ may be allowed. The latter metallicity provides a theoretical lithium abundance estimate consistent with observations. A lower metallicity model predicts too much lithium at 360 Myr. It should be possible to confirm each of these conclusions observationally.

3.3. CU Cancri

The variable M-dwarf CU Cancri (GJ 2069A, hereafter CU Cnc; Haro et al. 1975) was discovered to be a double-lined spectroscopic binary (Delfosse et al. 1998). Follow up observations provided evidence that CU Cnc underwent periodic eclipses, making it the third known M-dwarf DEB at the time (Delfosse et al. 1999). Shortly thereafter, Ribas (2003) obtained high-precision light curves in multiple photometric passbands. Combining his light curve data and the radial velocity data

from Delfosse et al. (1998), Ribas (2003) published a detailed reanalysis of CU Cnc with precise masses and radii for the two component stars. These values are presented in Table 1.

Initial comparisons with Baraffe et al. (1998) solar metallicity models indicated that the components of CU Cnc were 1 mag under luminous in the V band. Additionally, the prescribed spectral type was two subclasses later than expected for two 0.4 $M_{\odot}$ stars (M4 instead of M2; Delfosse et al. 1999). These oddities provided evidence that CU Cnc may have a super-solar metallicity. An increased metallicity would increase TiO opacity at optical wavelengths producing stronger TiO absorption features used for spectral classification. Absolute V band magnitudes would also be lowered since TiO bands primarily affect the opacity at optical wavelengths, shifting flux from the optical to the near-infrared. Using Baraffe et al. (1998) models with metallicity 0.0 and −0.5, Delfosse et al. (1999) performed a linear extrapolation to estimate a metallicity of [Fe/H] $\sim +0.5$.

A super-solar metallicity, as quoted by Delfosse et al. (1999), is supported by the space velocity of CU Cnc. It has galactic velocities $U \approx -9.99$ km s^{-1}, $V \approx -4.66$ km s^{-1}, and $W \approx -10.1$ km s^{-1} and is posited to be a member of the thin-disk population. This population is characterized by younger, more metal-rich stars. However, space velocities were used by Ribas (2003) to refute the Delfosse et al. (1999) metallicity estimate. Instead of indicating that CU Cnc has a super-solar metallicity, Ribas conjectured that the space velocities of CU Cnc implied it was a member of the CMG. The CMG is defined by $U = -10.6 \pm 3.7$ km s^{-1}, $V = -6.8 \pm 2.3$ km s^{-1}, and $W = -9.4 \pm 2.1$ km s^{-1}. Therefore, Ribas prescribed the metallicity of the Castor system to CU Cnc (see Section 3.2), suggesting that CU Cnc may have a near-solar or slightly sub-solar metallicity.

With a metallicity and age estimate defined by the CMG, Ribas (2003) performed a detailed comparison between stellar models and the observed properties of CU Cnc. Models of the CU Cnc stars were found to predict radii 10%–14% smaller than observed. Furthermore, effective temperatures were 10%–15% hotter than the effective temperatures estimated by Ribas (2003). CU Cnc was found to be under luminous in the V and K band by 1.4 mag and 0.4 mag, respectively. Ribas proceeded to lay out detailed arguments that neither stellar activity nor metallicity provides a satisfactory explanation for the observed radius, $T_{\rm eff}$, and luminosity discrepancies. Instead, he proposes that CU Cnc may possess a circumstellar disk. The disk would then disproportionately affect the observed V band flux compared to the K band. This would also force the effective temperatures to be reconsidered, leading to a change in the observed luminosities.

Ribas (2003) relies heavily on the estimated effective temperature of the individual components. Determining M-dwarf effective temperatures is fraught with difficulty. There is a strong degeneracy between metallicity and effective temperature for M-dwarfs when considering photometric color indices. We will therefore return to a detailed discussion of the luminosity discrepancies later and focus on the radius deviations first. Radius estimates will be less affected by the presence of a circumstellar disk since radius determinations rely on differential photometry.

In Feiden & Chaboyer (2012a), our models preferred a super-solar metallicity when attempting to fit CU Cnc. The maximum metallicity permitted in that analysis was [Fe/H] = +0.2 dex. Since CU Cnc may have a metallicity greater than the limit in Feiden & Chaboyer (2012a), we begin with a standard model analysis of CU Cnc assuming a super-solar metallicity with

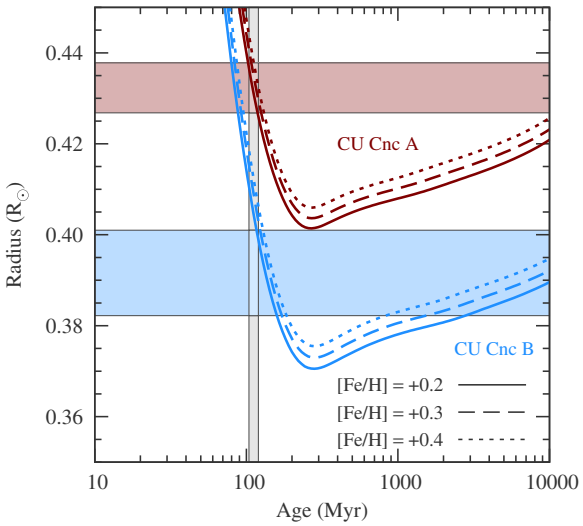

Figure 7. Standard Dartmouth mass tracks for CU Cnc A (maroon) and CU Cnc B (light-blue) at three different metallicities: +0.2 (solid), +0.3 (dashed), +0.4 (dotted). Horizontal bands identify the observed radius with 1σ uncertainty while the vertical band identifies the region in age–radius space where the models match the primary star's observed radius.

(A color version of this figure is available in the online journal.)

[Fe/H] $\geqslant +0.2$ dex. Allowing for CU Cnc to have a super-solar metallicity, or in particular a metallicity different from YY Gem, contradicts its proposed membership with the CMG. However, even though CU Cnc has a similar velocity to Castor (within 3 km s^{-1}), other proposed members of the CMG have been shown to differ significantly from Castor (and each other) in their velocities (Mamajek et al. 2013). Mamajek et al. (2013) present detailed arguments that show the motions of CMG members are dominated by the Galactic potential, meaning members very likely do not have a common birth site. While CU Cnc may have common properties with Castor, it is far from certain whether the two share a common origin. Therefore, we reject the CMG association, thus allowing for age and metallicity to be free parameters in our modeling.

Standard stellar evolution models of both components are presented in Figure 7. Results are nearly independent of the adopted metallicity. All mass tracks show that the models do not match the observed stellar radii at the same age along the MS. Models of the primary appear to deviate from the observations more than models of the secondary. This may just be a consequence of the larger radius uncertainty quoted for the secondary star, creating an illusion of better agreement. Quoting precise values for the level of disagreement is difficult as it depends strongly on the adopted age. Assuming an age of 360 Myr, our models under predict the radius of the primary and secondary by 7% and 5%, respectively.

Agreement between the models and observations for both components is seen near 120 Myr (vertical shaded region in Figure 7). At this age, the stars are undergoing gravitational contraction along the pre-MS. We cannot rule out the possibility that the stars of CU Cnc are still in the pre-MS phase. Ribas (2003) tentatively detects lithium in the spectrum of CU Cnc, which strongly suggests it is a pre-MS system. However, models predict complete lithium depletion around 20 Myr, 100 Myr prior to where the models show agreement. This is almost entirely independent of metallicity. Only by drastically lowering the metallicity to −1.0 dex are we able to preserve some lithium at the surface of CU Cnc A as it reaches the MS. We note also

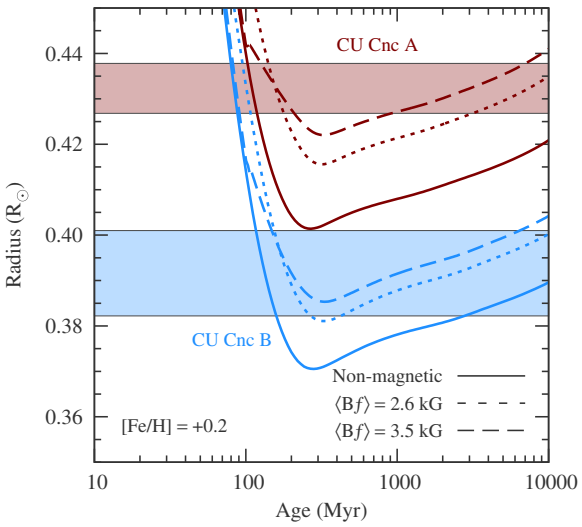

Figure 8. Magnetic stellar evolution mass tracks of CU Cnc A (maroon) and CU Cnc B (light-blue) with surface field strengths of 2.6 kG (dotted) and 3.5 kG (dashed). A non-magnetic mass track for each star is shown as a solid line. All models have [Fe/H] = +0.2 following the discussion in the text. The horizontal swaths signify the observed radius with associated 1σ uncertainty.

(A color version of this figure is available in the online journal.)

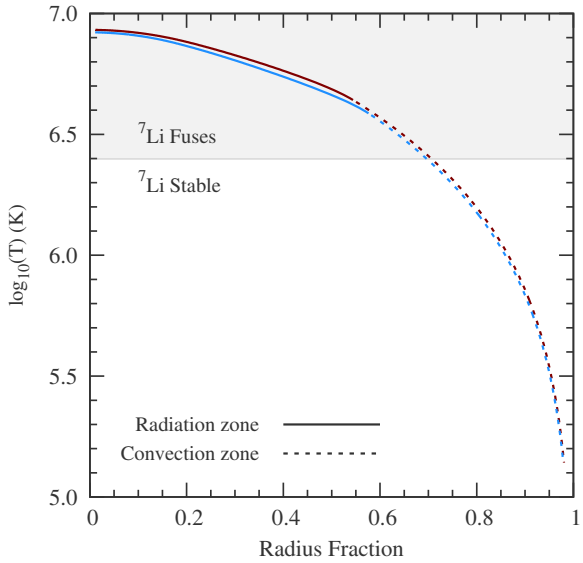

Figure 9. Temperature profile within a standard (maroon) and magnetic (light-blue) model of CU Cnc A showing that the base of the convection zone exists at a higher temperature than the ^{7}Li fusion temperature (gray shaded area above $\log(T) = 6.4$). The influence of the magnetic field on the location of the convection zone base can be seen. Note that the temperature profile from the stellar envelope calculation is not included.

(A color version of this figure is available in the online journal.)

that agreement between the models and observations occurs right at the edge of the gray vertical area in Figure 7, suggesting that the agreement may be spurious.

For the purposes of this study, we assume that the stars have reached the MS and that magnetic fields may underlie the observed radius discrepancies. There is evidence that the stars are magnetically active. *ROSAT* observations show strong X-ray emission[6] (López-Morales 2007; Feiden & Chaboyer 2012a) indicative of the stars having magnetically heated coronae. CU Cnc is also classified as an optical flare star that undergoes frequent flaring events (Haro et al. 1975; Qian et al. 2012). Furthermore, the stars show strong chromospheric Balmer and Ca II K emission during quiescence (Reid et al. 1995; Walkowicz & Hawley 2009). These tracers point toward the presence of at least a moderate level of magnetic activity on the stellar surfaces.

Magnetic models were computed using a dipole magnetic field profile and two surface magnetic field strengths were chosen, 2.6 kG and 3.5 kG. Mass tracks including a magnetic field are shown in Figure 8. We fixed the metallicity to [Fe/H] = +0.2 since it makes only a marginal difference in the overall radius evolution of standard model mass tracks. Note that the magnetic perturbation time is different between the 2.6 kG and 3.5 kG tracks. The perturbation age was pushed to 100 Myr when using a 3.5 kG model to ensure model convergence immediately following the perturbation. We performed numerical tests to confirm that altering the perturbation age does not influence results along the MS.

Figure 8 shows that our model of the secondary star with a surface magnetic field strength of 3.5 kG matches the observed radius between 300 Myr and 6 Gyr (ignoring the pre-MS). A lower, 2.5 kG, surface magnetic field strength produces similar results, but shows slight disagreement with the observations near the zero-age main sequence (ZAMS) at 300 Myr. However, the 2.5 kG model extends the maximum age from 6 Gyr to 10 Gyr. Unlike models of the secondary, neither of the magnetic models of the primary produce agreement near the ZAMS. Instead, agreement is obtained between 900 Myr and 6 Gyr. To create agreement between the model and observed radius near the ZAMS, our models would require a stronger surface magnetic field strength.

The need for a stronger magnetic field in the primary depends on the real age of the system. Ribas (2003) invoked the possible CMG membership to estimate an age. The CMG is thought to be approximately 350–400 Myr (see Section 3.2). According to Figure 8, this would place CU Cnc near the ZAMS. It also means that a stronger magnetic field would be needed in modeling the primary star. In fact, a surface magnetic field strength of 4.0 kG is required to produce agreement with the primary if CU Cnc is coeval with the CMG. However, there is no compelling argument that leads us to believe that CU Cnc has properties in common with Castor. Kinematic similarities among field stars is not sufficient for assigning a reliable age or metallicity (e.g., Mamajek et al. 2013).

If CU Cnc is a young system near the ZAMS, a magnetic field may hinder lithium depletion from the stellar surface. We saw that this occurred with YY Gem in Section 3.2. However, depletion of lithium from the surface of the stars in CU Cnc is unaffected by a strong magnetic field. Unlike YY Gem, where lithium was preserved to a significantly older age, the stars in CU Cnc destroy lithium along the pre-MS, nearly independent of metallicity and magnetic field strength. This can be readily explained by the depth of the convective envelope in the stars of CU Cnc. At $\sim$0.4 $M_\odot$, the stars are expected to have deep convection zones that extend from the stellar surface down to about 55% of the stellar radius. Lithium is destroyed ($T = 2.5 \times 10^6$ K) at a depth located considerably closer to the stellar surface than the convection zone boundary. This is illustrated in Figure 9. Lithium will be mixed down to the base of the convection zone where it will rapidly burn, leading to a complete absence of lithium by 20 Myr. Introducing a strong magnetic field (3.5 kG) reduces the size of the convection zone in CU Cnc A by 7% and by 9% in CU Cnc B. In contrast,

[6] *ROSAT* observations actually contain emission from both CU Cnc and its proper motion companion, the spectroscopic binary CV Cnc.

to preserve lithium the size of the convection zone would have to be reduced by nearly 30%. This corresponds to the base of the convection zone moving from 55% to 70% of the total stellar radius. If lithium exists at the surface of CU Cnc, then there is another process keeping lithium from being destroyed.

We conclude this section on CU Cnc by returning to the photometric issues raised by both Delfosse et al. (1999) and Ribas (2003). Since the publication of Ribas (2003), *Hipparcos* parallaxes have been revised and updated to provide more accurate solutions (van Leeuwen 2007). The parallax for CU Cnc underwent a revision from $\pi = 78.05 \pm 5.69$ mas to $\pi = 90.37 \pm 8.22$ mas, changing the distance estimate from 12.81 ± 0.92 pc to 11.07 ± 1.01 pc. Absolute magnitudes must be adjusted for this revised distance. Using *V*- and *K*-band magnitudes listed in Weis (1991)[7] and the Two Micron All Sky Survey (2MASS) archive (Cutri et al. 2003), we find $M_{V,A} = 12.27$ mag, $M_{V,B} = 12.63$ mag, and an integrated $M_K = 6.382$ mag. From SIMBAD we obtain integrated colors: $(J-K) = 0.906$ and $(H-K) = 0.291$, drawn from the 2MASS survey.

Using theoretical color-$T_{\rm eff}$ transformations (Dotter et al. 2007, 2008) we convert model surface properties to photometric magnitudes and colors. We were unable to reproduce the set of integrated colors and magnitudes or the individual *V*-band magnitudes using super-solar metallicity models alone. However, combining a super-solar metallicity with a magnetic field, we were able to produce models showing the appropriate trends: total *V*- and *K*-band magnitudes were reduced due to the decrease in luminosity associated with a magnetic field. There was a steeper decrease in the *V*-band due to increased metallicity and decreased $T_{\rm eff}$ due to both metallicity and a magnetic field. The final photometric properties of our models did not exactly match the properties of CU Cnc. We note there is considerable uncertainty in the color-$T_{\rm eff}$ transformation using the PHOENIX AMES-COND theoretical models (Baraffe et al. 1998; Delfosse et al. 1998), particularly in the *V*-band. A larger exploration of the model parameter space and upgrading to the latest PHOENIX BT-SETTL models would help to determine if metallicity and magnetic fields are able to resolve the CU Cnc photometric anomalies. Whether a dusty disk exists should be testable using photometric data from *WISE* (Wright et al. 2010), which may reveal excess infrared emission.

4. MAGNETIC FIELD STRENGTHS

Section 3 demonstrates that introducing a magnetic perturbation within stellar models can reconcile the model predictions with observations of low-mass stars in DEBs. But, the real predictive power of the models relies on their ability to do so with realistic magnetic field strengths. Better yet, with magnetic field strengths that translate into physical observables. In Feiden & Chaboyer (2012b), we showed that it was possible to test the validity of magnetic models using the stellar X-ray luminosity. Magnetic models of EF Aquarii appeared to be consistent with this analysis. We perform a similar analysis for the stars studied in this paper.

4.1. Estimating Surface Magnetic Field Strengths

Estimates of surface magnetic field strengths can be obtained using an empirical scaling relation derived between the total X-ray luminosity (L_x) of a star and its surface magnetic flux (Φ) (Fisher et al. 1998; Pevtsov et al. 2003). The relation states that (Pevtsov et al. 2003)

$$L_x \propto \Phi^p, \tag{2}$$

where $p = 1.15$, and appears to extend over 12 orders of magnitude in Φ and L_x. This includes data from individual solar quiet regions, solar active regions, and hemispherical averages from single field stars, among others. However, the adopted power-law index does show variation between the individual data sets. For example, Pevtsov et al. (2003) found a power-law index of $p = 0.98$ when they only considered dwarf star data from Saar (1996). This is quite different from the power-law index of $p = 1.15$ derived when analyzing the ensemble of observations.

The question of which power law index to adopt is important and can strongly influence the magnetic flux derived from X-ray luminosities. Seeing as we are focused on deriving the approximate magnetic flux for dwarf stars, it seems a natural choice to use the relation specifically derived from dwarf star data. The relation derived by Pevtsov et al. (2003) was based on magnetic field measurements presented by Saar (1996). Since then, many more stars have had their surface magnetic field strengths measured (see Donati & Landstreet 2009; Reiners 2012 for reviews).

We have re-derived the empirical scaling relation with this expanded data set (see the Appendix). The updated relation is shown in Figure 10, where we find that

$$\log_{10}\Phi = (11.86 \pm 0.68) + (0.459 \pm 0.018)\log_{10} L_x. \tag{3}$$

Note that we have reversed the axes from how the relation was originally presented by Fisher et al. (1998). This is because we are interested in predicting Φ from a measure of L_x instead of establishing a casual relationship between the two quantities.

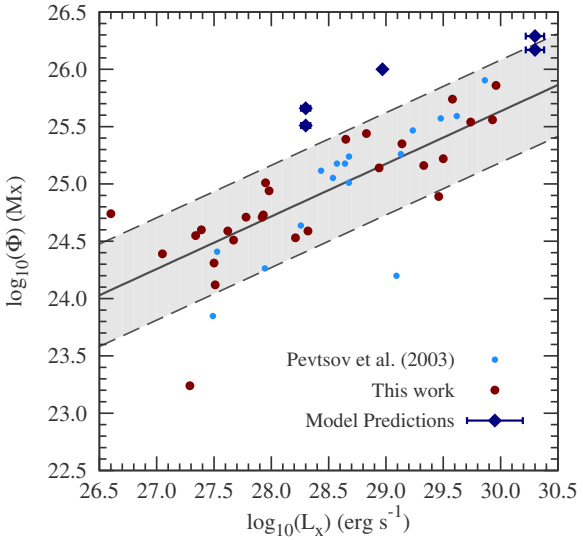

Figure 10. Unsigned stellar surface magnetic flux (Φ) as a function of the total stellar X-ray luminosity for a collection of G-, K-, and M-dwarfs. Data shown are from Pevtsov et al. (2003) (small, gray points), this work (large, maroon points), and theoretical predictions from this work (blue, diamonds).
(A color version of this figure is available in the online journal.)

4.2. Surface Magnetic Field Strengths

X-ray properties of the three DEBs analyzed in this study are determined using X-ray data from the *ROSAT* All-Sky Survey

[7] The integrated *V*-band magnitude listed on SIMBAD is 0.2 mag fainter than is quoted by Weis (1991). This is probably because the photometry listed on SIMBAD was taken during an eclipse, where the *V*-band flux drops by ~ 0.2 mag (Ribas 2003).

Table 3
X-Ray Properties for the Three DEB Systems

DEB System	X_{cr} (counts s^{-1})	HR	π (mas)	N_{stars}	L_x (erg s^{-1})
UV Psc	0.92 ± 0.07	-0.10 ± 0.07	14.64 ± 1.03	2	$(2.0 \pm 0.3) \times 10^{30}$
YY Gem	3.70 ± 0.09	-0.15 ± 0.02	$d = 13 \pm 2$ pc	6	$(9.4 \pm 0.2) \times 10^{28}$
CU Cnc	0.73 ± 0.05	-0.14 ± 0.06	90.37 ± 8.22	4	$(2.0 \pm 0.2) \times 10^{28}$

Notes. N_{stars} is the total number of stars thought to be contributing to the total X-ray counts detected by *ROSAT*. The value L_x is quoted as the X-ray luminosity per star in the system.

Table 4
Surface Magnetic Field Properties for UV Psc, YY Gem, and CU Cnc

DEB Star	$\log \Phi$ (Mx)	$\langle Bf \rangle$ (kG)	$\langle Bf \rangle_{model}$ (kG)
UV Psc A	25.77 ± 0.45	$0.79^{+1.43}_{-0.51}$	2.0
UV Psc B	...	$1.39^{+2.53}_{-0.90}$	4.6
YY Gem A	25.16 ± 0.45	$0.62^{+1.13}_{-0.40}$	4.3
YY Gem B	...	...	...
CU Cnc A	24.85 ± 0.45	$0.62^{+1.13}_{-0.40}$	4.0
CU Cnc B	...	$0.76^{+1.38}_{-0.49}$	3.6

Bright Source Catalogue (Voges et al. 1999). *ROSAT* count rates (X_{cr}) and hardness ratios (HRs) are given in Table 3. We convert to X-ray fluxes using the calibration of Schmitt et al. (1995). The conversion to X-ray fluxes is complicated by the fact that *ROSAT* has relatively poor spatial resolution, meaning any nearby companions to these DEBs may also be contributing to the total X_{cr}.

The X-ray flux quoted in Table 3 is therefore calculated as the estimated flux per star, determined by dividing the total flux by the number of stars thought to be contributing to X_{cr}. This is not a problem for UV Psc, which appears isolated. YY Gem and CU Cnc, on the other hand, have known, nearby companions. A search of the *ROSAT* Bright Source Catalogue for Castor A and B yield the same data as is found when searching for YY Gem, indicating that *ROSAT* cannot spatially resolve these three systems. Castor A and B are both binaries, thought to have M-dwarfs companions, meaning that *ROSAT* is detecting X-ray emission from up to six sources. Similarly, CU Cnc has a 12″ companion, CV Cnc, another M-dwarf binary system. Both systems are likely contributing to the X_{cr} listed in the *ROSAT* Bright Source Catalogue.

Distances to the systems are calculated using updated *Hipparcos* parallaxes (van Leeuwen 2007), except for YY Gem, for which no parallax is available. Instead, we adopt a distance of 13 ± 2 pc, which has been estimated from earlier investigations (Chabrier & Baraffe 1995; López-Morales 2007; Feiden & Chaboyer 2012a). The distances allow for the calculation of the total X-ray luminosity per star, which we quote in Table 3.

Our estimates for the DEB surface magnetic fluxes, surface magnetic field strengths, and their associated errors are given in Table 4. We also include the surface magnetic field strengths required by our models for comparison. The X-ray data reveal that the magnetic field strengths required by our models are probably too strong. We demonstrate this visually by the dark blue diamond symbols in Figure 10. Since the magnetic models reproduce the observed stellar radii, the surface area of the model is equal to the observed stellar surface area. Thus, the larger magnetic fluxes observed from the models suggest the magnetic field strengths are too strong.

The data suggest that the only realistic magnetic field strengths may be those of UV Psc. However, the data points for UV Psc lie outside the domain of the empirical data set. Whether this extrapolation is valid remains unclear. Even if we assume the extrapolation is valid, UV Psc B lies just above the 1σ error bounds of the linear correlation. Conversely, UV Psc A lies just inside the boundary. We must therefore be cautious with our interpretation of the accuracy of our models for UV Psc. This is further reinforced by noting that only two G-dwarfs (the spectral type of UV Psc A) were included in the data set and are therefore under represented. Direct measurements of G-dwarf surface magnetic field strengths show they are around 500 G (Saar 1990). This is consistent with the surface magnetic field strength derived for UV Psc A from the X-ray luminosity relation, but inconsistent with our model predictions.

What is clear from Figure 10 and Table 4 is that the magnetic field strengths required by the models are too strong for the stars in YY Gem and CU Cnc. The models of YY Gem need a magnetic field strength that are a factor of six too strong. Similarly large magnetic fields are needed by the models for the stars of CU Cnc. Taking a more qualitative approach, the magnetic field strengths required by our models for YY Gem and CU Cnc appear within the realm of possibility. Numerous studies of M-dwarfs find that surface magnetic strengths of a few kilogauss are quite common (Saar 1996, 2001; Reiners & Basri 2007, 2009). However, these DEBs would then have noticeably stronger magnetic fields for their observed X-ray luminosity than the rest of M-dwarf population. It appears that our approach to modeling magnetic fields in low-mass stars may be incomplete.

4.3. Interior Magnetic Field Strengths

Assessing the validity of our predicted interior magnetic field strengths is inherently more difficult. There is currently no reliable method for measuring the magnetic field strengths present inside stars. Therefore, we elect to compare the theoretical magnetic field strengths required by our models with those predicted by 3D MHD models (see, e.g., Brandenburg & Subramanian 2005).

Table 5 presents the peak interior magnetic field strengths for the models presented above for both the dipole and the Gaussian field profiles (see below). The peak magnetic field strengths in Table 5 are pre-defined to be at the base of the stellar convection zone (Feiden & Chaboyer 2012b). They are all $\sim 10^3$ G to $\sim 10^4$ G. By comparison, 3D MHD models routinely find peak magnetic field strengths of a few times 10^3 G (consistent with equipartition estimates) to $\sim 10^5$ G for solar-like stars (see review by Brandenburg & Subramanian 2005). In the immediate context, "solar-like" is loosely taken to mean stars with a radiative core and a solar-like rotation profile. The peak magnetic field strengths of our models appear consis-

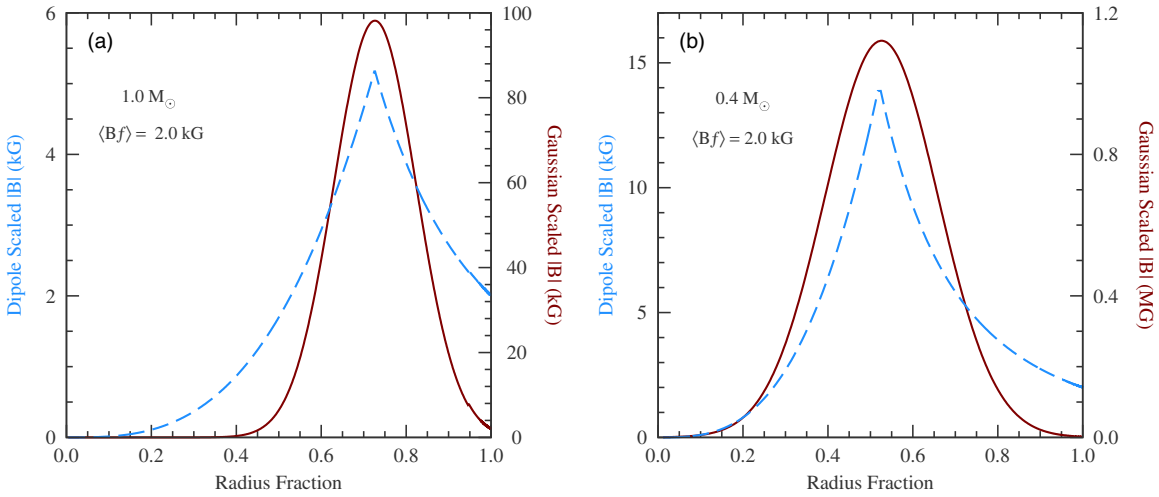

Figure 11. Comparison of the dipole (light blue, dashed) and Gaussian (maroon, solid) radial profiles for the interior magnetic field strength. (a) A 1.0 $M_{\odot}$ model. (b) A 0.4 $M_{\odot}$ model. Note that the two field profiles are plotted on different scales with the dipole on the left *y*-axis and the Gaussian on the right *y*-axis.
(A color version of this figure is available in the online journal.)

Table 5
Model Peak Interior Magnetic Field Strengths

DEB Star	$\lvert B\rvert_{\rm dipole}$ (kG)	$\lvert B\rvert_{\rm Gaussian}$ (kG)
UV Psc A	4	40
UV Psc B	12	400
YY Gem A	13	500
YY Gem B	...	...
CU Cnc A	21	1500
CU Cnc B	21	2000

tent with those predicted from 3D MHD models. Furthermore, while helioseismic investigations have yet to reveal the interior magnetic field profile for our Sun, initial indications suggest the peak magnetic field strength is below 300 kG (Antia et al. 2000). Estimates place the strengths in the vicinity of several tens of kG (Antia et al. 2003).

4.4. Reducing the Magnetic Field Strengths

Given the results that the model surface field strengths are likely too strong, we seek to reformulate our magnetic perturbation. We first consider some of the assumptions used to formulate our magnetic models presented in Feiden & Chaboyer (2012b) and used in Section 3. We have identified three key assumptions: (1) our prescribed magnetic field radial profile, (2) that convective elements are spherical and that the plasma obeys the equations of ideal magnetohydrodynamics (MHD), and (3) that the dynamo is driven completely by rotation.

4.4.1. Magnetic Field Radial Profile

In the models presented up to this point, we have followed the formulation described in Feiden & Chaboyer (2012b). There, we arbitrarily assumed that the magnetic field strength radial profile was a dipole configuration falling off as r^3 from a pre-defined peak field strength location. The location of the peak magnetic field strength was taken to be at the base of the convective envelope, nominally the stellar tachocline. Note that in fully convective objects, the peak magnetic field strength is located at 0.15 $R_{\star}$ (Feiden & Chaboyer 2012b). It may be possible to reduce the required surface magnetic field strengths if we instead use steeper radial profile. This would produce a stronger magnetic field at the tachocline for a given surface magnetic field strength.

To this end, we define a Gaussian radial profile. The tachocline is still the location of the peak magnetic field strength, now defined to be the peak of a Gaussian distribution. The radial profile is then defined by

$$B(r) = B(R_{\rm src}) \exp\left[-\frac{1}{2}\left(\frac{R_{\rm src} - r}{\sigma_g}\right)^2\right] \quad (4)$$

where σ_g is the width of the Gaussian and $R_{\rm src}$ is the radial location of the tachocline. The adopted width of the Gaussian is arbitrary. In most applications, it would be reasonable to set the width of the Gaussian to a constant value. For instance, a value of $\sigma_g = 0.2$ was favored by Lydon & Sofia (1995). However, since we will be considering stars with varying convection zone depths (not only the Sun as in Lydon & Sofia 1995), we felt a single value would not be appropriate. Instead, we define σ_g as a function of the convection zone depth. This allows us to localize the magnetic field in thin convection zones and distribute the magnetic field in fully convective stars, thereby maintaining seemingly realistic values for the peak magnetic field strength (see Table 5). The width of the Gaussian was fixed to $\sigma_g = 0.2$ in fully convective objects and $\sigma_g = 0.1$ in the Sun. Therefore, we can define

$$\sigma_g = 0.2264 - 0.1776\,(R_{\rm src}/R_{\star})\,. \quad (5)$$

A direct comparison of the shape of the magnetic field profiles used in this study is given in Figure 11. Two masses are shown to make clear the variable width of the Gaussian.

Figure 12 illustrates the influence of using the Gaussian radial profile. We plot the relative difference in the radius evolution between the Gaussian and dipole radial profiles for a series of stellar masses. All of the models have an equivalent surface magnetic field strength of 2.0 kG and a solar metallicity. Despite the increased magnetic field strength at the tachocline (see Table 5 and Figure 12), using a Gaussian radial profile instead of a dipole profile has a largely sub-1% effect on model radius predictions. Therefore, we find no compelling reason to alter our default field strength profile.

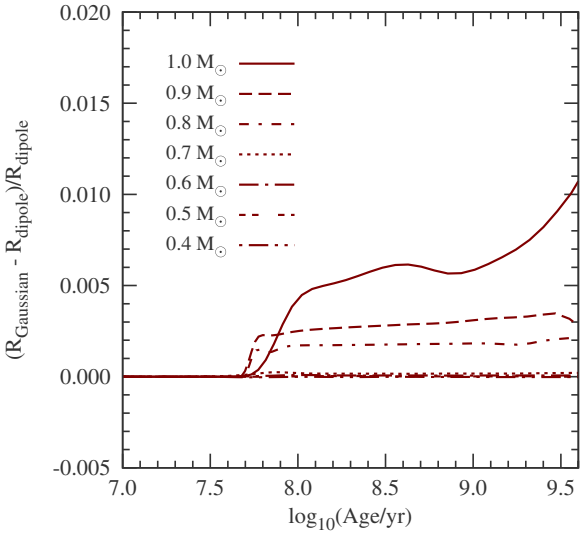

Figure 12. Effect on stellar radius predictions caused by using a Gaussian radial profile instead of a dipole profile. Shown is the relative radius difference as a function of age for a series of stellar models. All of the models have equivalent surface magnetic field strengths (2.0 kG) but different magnetic field radial profiles.

(A color version of this figure is available in the online journal.)

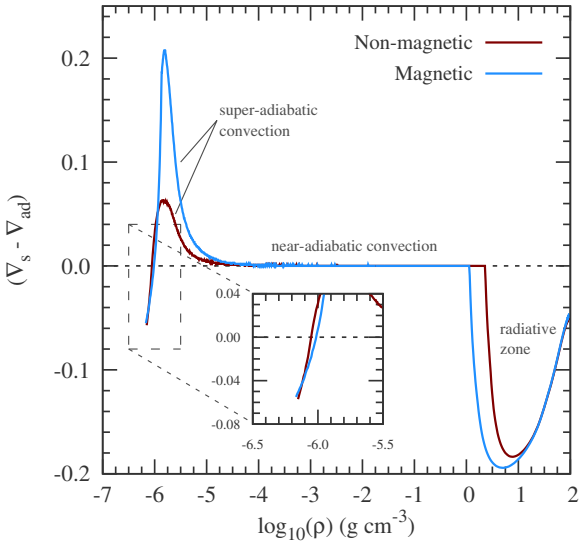

Figure 13. Difference between the plasma temperature gradient, ∇_s, and the adiabatic temperature gradient, ∇_{ad}, as a function of the logarithmic plasma density for a $M = 0.6\,M_\odot$ star. We show this for two models: a non-magnetic model (maroon, solid line) and a magnetic model (light blue, solid). The zero point is marked by a gray dashed line, dividing locations where convection (positive) or radiation (negative) is the dominant flux transport mechanism. The inset zooms in on the near-surface region where radiation becomes the dominant flux transport mechanism.

(A color version of this figure is available in the online journal.)

Two additional comments on the results presented in Figure 12. First, the two radial profiles produce similar results despite the peak magnetic field strengths differing by about an order of magnitude. It would seem that the deep interior field strength is relatively unimportant in stars with radiative cores. Instead, the surface magnetic field strength appears to be primarily responsible for driving the radius inflation. This is consistent with the previous study by Spruit & Weiss (1986).

To understand why, we plot the difference between the temperature gradient of the ambient plasma, ∇_s, and the adiabatic gradient, ∇_{ad}, as a function of density in Figure 13. Consider the non-magnetic model. When the line dips below the zero point, radiation carries all of the excess energy. Near the stellar surface, where the density, ρ, is small, ∇_s is noticeably super-adiabatic, indicative of inefficient convective energy transport. Deeper in the star, where $-5 < \log_{10}\rho < 0$, the temperature gradient is super-adiabatic, but only slightly ($\nabla_s - \nabla_{ad} < 10^{-8}$). This suggests convective energy transport is highly efficient.

Our magnetic field implementation modifies ∇_{ad} by a factor proportional to $\nu\nabla_\chi$, where

$$\nu\nabla_\chi = \frac{P_{mag}}{P_{gas} + P_{mag}} \left(\frac{d \ln \chi}{d \ln P} \right). \quad (6)$$

In Equation (6), $\nu = -(\partial \ln \rho / \partial \ln \chi)$ at constant P and T, a magnetic compression coefficient, and ∇_χ is the gradient of the magnetic energy per unit mass, χ ($= B^2/8\pi\rho$), with respect to the total pressure, P (also see Equation (11)). Deep in the stellar interior, $\nabla_\chi \sim 0.1$, and $\nu \sim 10^{-8}$–10^{-9}. This is not sufficient to inhibit convection deep within the star. The exact situation can be more complicated and is discussed further in Section 5. Near the surface, however, any inhibition of convection causes a steepening of ∇_s, forcing radiation to carry more energy. We then expect to see a growth of the region near the stellar surface where radiation carries all of the flux, as is seen in Figure 13. The structural changes caused by the steep temperature gradient near the surface are enough to reconcile the models with the observations before the deep interior magnetic field strength becomes appreciable in magnitude so as to inhibit convection. Therefore, the outward movement of the convection zone boundary occurs largely as a response to changes near the stellar surface.

Next, we see in Figure 12 that the $1.0\,M_\odot$ track displays a sharp upturn near 1 Gyr. The model is too young to be undergoing rapid evolutionary changes. Instead, we believe this is related to the physical properties of the star near the boundary of the convection zone. As we just discussed, the magnetic field strengths for both profiles are typically too weak near the tachocline to affect stellar structure. However, this is not true for a $1.0\,M_\odot$ model. The convection zone is thin and convection is generally super-adiabatic throughout. This results in the Gaussian radial profile having a stronger effect on the properties of convection. We now also see why the Gaussian radial profile has a weaker influence on the stellar radius as we decrease the stellar mass. Convection in the deep interior becomes more adiabatic (re: efficient) at lower masses.

4.4.2. The Free Parameter, f

The technique advanced by Lydon & Sofia (1995) introduces a number of free parameters that govern the interaction between an imposed magnetic field and the stellar plasma. One of these parameters, γ, governs the amount of pressure exerted on the plasma by a magnetic field and was investigated in Feiden & Chaboyer (2012b). Another parameter, f, controls the relationship between the magnetic energy gradient of a convecting element and that of the surrounding plasma. Physically, f is related to the geometry of the convecting element and the conductivity of the plasma. For instance, assuming that convecting elements are spherical and that the plasma is infinitely conducting, we found that $f \approx 1$ (Feiden & Chaboyer 2012b). Although stellar interiors may be considered, for all practical purposes, infinitely conducting, this is not necessarily the case in the stellar envelope.

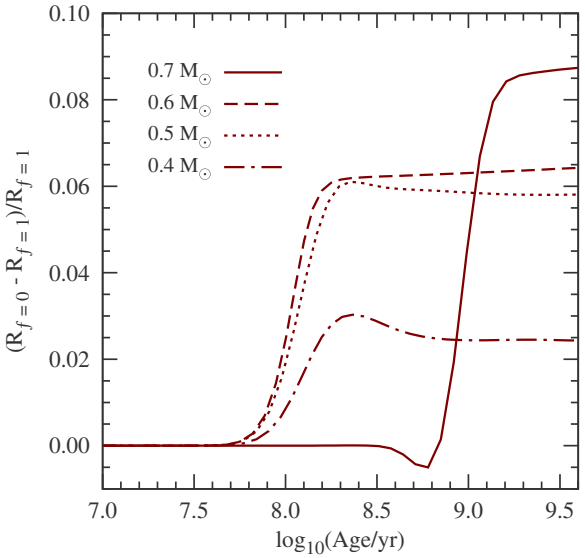

Figure 14. Influence of the parameter f on model radius predictions. Plotted is the relative difference in radius evolution between magnetic models computed with $f = 1$ and $f = 0$. All models have a prescribed surface magnetic field strength of 2.0 kG.

(A color version of this figure is available in the online journal.)

Changing f so that it is no longer fixed to 1 introduces an additional term in the convective buoyancy equation. This term can either increase or decrease the buoyancy force felt by a convecting element, depending on the sign of the plasma magnetic energy gradient and the precise value of f (see Equation (57) in Feiden & Chaboyer 2012b). In our studies, the magnetic energy gradient is decreasing toward the model center throughout the stellar envelope. Thus, decreasing f from 1 slows the buoyant motion of a convective element thereby reducing the convective flux.

Instead of attempting to physically motivate a value for f, we take the approach of testing an extremal value. By setting $f = 0$ we maximize the Lorentz force term mentioned above, given our radial profile. Results of changing the value of f from $f = 1$ to $f = 0$ are shown in Figure 14. As with Figure 12, we plot the relative difference in the radius evolution for a series of mass tracks. All of the models were calculated with a 2.0 kG magnetic field and a dipole field profile (see the previous section). The largest mass model shown is $0.7\,M_{\odot}$ as models with larger masses failed to converge for a 2.0 kG magnetic field with $f = 0$. It is evident from Figure 14 that lowering the value of f can have a significant impact on the model radius evolution. Differences between 2% and 9% were observed, depending on the mass of the model. Therefore, it is worthwhile to study the effect of setting $f = 0$ on the individual DEB stars discussed above.

Setting $f = 0$ reduced the magnetic field strengths required to reconcile model radii by about half. The model of YY Gem, for instance, only requires a surface magnetic field strength of 2.5 kG compared to the 4.3 kG required with $f = 1$. However, the reduced surface magnetic field strengths are still too strong compared with values estimated from X-ray emission. Models of UV Psc are in better agreement with the X-ray predicted values, but we have already given reasons to be skeptical of these predictions.

Whether or not we have reason to believe that f should be zero is a more difficult question. Geometric considerations about convecting elements have long been debated in standard MLT, but they ultimately have little impact on model predictions (Henyey et al. 1965). However, when considering magnetic MLT, convective element geometry may come to matter. Quantifying the effects of plasma conductivity on f is far more difficult. It is safe to assume that the stellar plasma is highly conducting throughout a majority of the stellar interior, where temperatures exceed 10^4 K and hydrogen is completely ionized. Near the surface, free electrons from hydrogen ionization are no longer available, meaning conductivity is decreased, but not necessarily zero. Free electrons from other species (e.g., Ca and Na) keep the plasma at least partially conducting. Physically motivating an expression for f in terms of the plasma conductivity and convective bubble geometry would be a worthwhile endeavor. We plan to investigate this in a future study. Ultimately, we have shown that the value of f, while of consequence, does provide enough leverage to bring our models into agreement with the observations using realistic surface magnetic field strengths.

4.4.3. Dynamo Energy Source

The final assumption that we identified was that the magnetic field is "driven" completely by rotation. By doing so, we have allowed for the unintended consequence that the magnetic field strength—both the surface and the interior—can grow without limit.[8] There is no natural limit imposed upon the field strengths as the mechanism from which the field is drawing energy (i.e., rotation) is neglected entirely.

Limiting the magnetic field strengths, however, does not alter the ease by which a magnetic field can induce stellar inflation. What it can do is validate or invalidate the required surface magnetic field strengths. However, if we reconsider the physical source of the magnetic field, it can lead to new methods of including magnetic fields in stellar evolution codes. There are questions as to whether the solar magnetic field is generated at the tachocline by the strong shear induced by rotation (i.e., the standard Parker model; Parker 1955) or if it is primarily generated within the solar convection zone by turbulent convection without explicit need for a tachocline (Brandenburg & Subramanian 2005; Brown et al. 2010).

Generation of a magnetic field from turbulent convection would suppress convective velocity fluctuations thereby reducing the total heat flux transported by convection. Early three-dimensional magneto-convection simulations support this assessment (Stein et al. 1992). Given that thick convective envelopes are a ubiquitous feature of low-mass stars, it is not unreasonable to posit that suppressing the total heat flux transported by convection would strongly impact stellar structure.

Assuming that the magnetic field sources its energy directly from the kinetic energy of turbulent convection has important consequences for a magnetic theory of convection. Consider a single convecting bubble. If the bubble is traveling with some velocity, $u_{\mathrm{conv},0}$, it has a kinetic energy equal to $\rho u^2_{\mathrm{conv},0}/2$, where ρ is the mass density of the plasma. Now, suppose some of that kinetic energy is used to generate the local magnetic field. By conservation of energy, we must have that

$$\frac{1}{2}\rho u^2_{\mathrm{conv},0} = \frac{1}{2}\rho u^2_{\mathrm{conv}} + \frac{B^2}{8\pi}, \tag{7}$$

where u_{conv} is the convective velocity after generation of a magnetic field and the final term is the magnetic energy. We have

[8] We note that there is a computational limit whereby too strong of a magnetic field will prevent the model from converging to a solution. This occurs slightly after the magnetic pressure exceeds the gas pressure near the photosphere.

implicitly assumed that a characteristic convecting bubble is responsible for generating the magnetic field only in its vicinity. This local treatment is a purely phenomenological approach and gives an upper limit to the effects of a turbulent dynamo, but provides a reasonable zeroth-order approximation within the framework of MLT.

The result is that the characteristic convective bubble will have a lower velocity in the presence of a magnetic field,

$$u_{\rm conv}^2 = u_{\rm conv,\,0}^2 - u_A^2. \tag{8}$$

The last term on the right hand side is equal the square of the local Alfvén velocity,

$$u_A^2 = \frac{B^2}{4\pi\rho}. \tag{9}$$

The diversion of energy into the magnetic field can significantly reduce the total convective flux, as the convective flux is proportional to $u_{\rm conv}^3$. This reduction in convective flux forces the radiative temperature gradient to grow steeper by an amount proportional to u_A^2.

To include these effects, we re-derived the equations of MLT given in Feiden & Chaboyer (2012b). The convective velocity and convective flux were modified to account for the loss of energy to the magnetic field. Unfortunately, we were unable to find convergence when numerically solving the system of equations. Closer inspection of the coefficients in our new quartic equation (see Equation (65) in Feiden & Chaboyer 2012b) revealed that there was no real root in the outer portions of the stellar envelope. The low density present in the envelope drives up u_A^2, causing the range of our final equation to lie above zero for all real values of the convective velocity. We also attempted to modify the "non-adiabaticity" equation (Equation (58) in Feiden & Chaboyer 2012b) so as to model the transformation of turbulent kinetic energy into magnetic energy as an effective heat loss. However, we were again unable to obtain convergence for the resulting quartic equation. We are continuing the investigate this issue.

Instead, we opted to first solve the MLT equations as normal and then modify the results to mimic the conversion of turbulent kinetic energy to magnetic energy. The convective velocity is reduced by the Alfvén velocity, as in Equation (8). While energy is transferred to the magnetic field, we assume that the energy is still confined to the local region under consideration, thereby reducing the total flux of energy across the region. Assuming that energy flux is conserved, radiation must attempt to carry additional energy flux. This leads to an increase in the local temperature gradient of the ambient plasma that is proportional to the total energy removed from the convecting element. Specifically,

$$\Delta(\nabla_{\rm s} - \nabla_{\rm e}) \propto \frac{u_A^2}{C}, \tag{10}$$

where $C = g\alpha_{\rm MLT}^2 H_P \delta/8$ is the characteristic squared velocity of an unimpeded convecting bubble over a pressure scale height (H_P). In the definition of C, we find the local gravitational acceleration g, the convective mixing length parameter $\alpha_{\rm MLT}$, and the coefficient of thermal expansion $\delta = -(\partial \ln \rho/\partial \ln T)_{P,\,\chi}$. Increasing the temperature excess increases the buoyancy of a convective element, increasing its velocity. However, for now, we concern ourselves only with the simple first-order approximation and neglect the immediate feedback on the convective velocity.

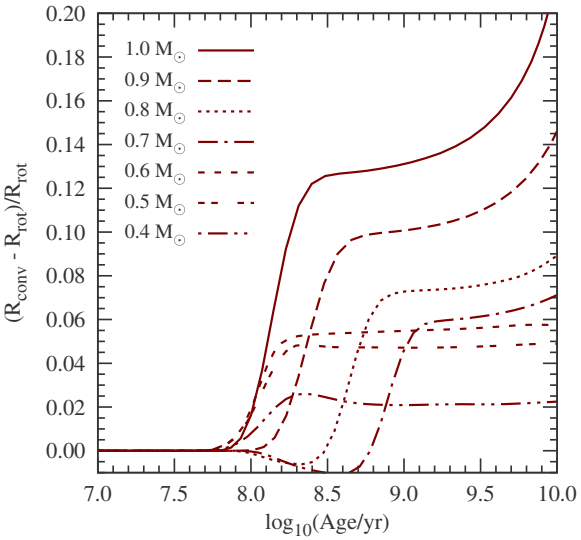

Figure 15. Effect on model radius predictions when the dynamo source is turbulent convection instead of purely rotation. Shown is the relative radius difference as a function of age for a series of stellar models. All of the models have an equivalent surface magnetic field strengths of 0.5 kG.

(A color version of this figure is available in the online journal.)

We again compute a series of models using this new modified MLT and compare the relative differences in radius evolution to our original formulation. These tracks are shown in Figure 15. We assume a 500 G surface magnetic field strength with a dipole radial profile and $f = 1$. Stabilization of convection, or a modified Schwarzschild criterion, is neglected, leaving only the reduction of convective flux to influence the convective properties. The 0.7 $M_\odot$, 0.8 $M_\odot$, and 0.9 $M_\odot$ tracks in Figure 15 show slightly different characteristics. Models assuming a turbulent dynamo readjusted to the presence of the magnetic field at an older age than did the models with the rotational dynamo. Despite appearances, all perturbations were introduced at an age of $\tau_{\rm age} = 0.1$ Gyr. It is apparent from Figure 15 that this new method of handling magneto-convection can significantly reduce the surface magnetic field strength required to inflate model radii.

We recomputed models for UV Psc, YY Gem, and CU Cnc using the best fit metallicities found in Section 3. We were able to achieve model convergence for the stars in YY Gem and CU Cnc. Models of the stars in UV Psc with surface magnetic fields greater than 650 G, required to correct the model radii, did not converge. We also recomputed models for EF Aquarii (Vos et al. 2012; Feiden & Chaboyer 2012b), but ran into the same convergence issues. We are continuing to investigate this issue. The resulting magnetic field strengths required for YY Gem and CU Cnc A and B were 0.7 kG, 0.7 kG, and 0.8 kG, respectively.

The surface magnetic field strengths derived from sourcing the magnetic field energy from convection are nearly identical to the value estimated from X-ray emission. This agreement lends credence to our latest approach, at least for lower mass models. We found it difficult to attain model convergence using this approach for models with masses greater than about 0.75 $M_\odot$. Stronger magnetic fields were required than could be achieved with the present model configuration. This was a consequence of the Alfvén velocity exceeding the convective velocity at some point within the convective envelope. Below that approximate

mass limit the turbulent dynamo approach can inflate stellar radii with relative ease compared to our original formulation. Whether this is indicative of the actual dynamo processes acting in each star is not clear. It is thought that the dynamo mechanism begins shifting from a rotationally driven dynamo to a turbulent dynamo somewhere around 0.6 $M_\odot$ (early-M; pg. 228 in Reid & Hawley 2005, and references therein), which would suggest YY Gem has a predominantly rotational dynamo. We explore possible tests to delineate between the two processes using stellar models in the next section.

5. DISCUSSION

5.1. Interior Structure

Section 4.4.3 presents a second approach to modeling the effects of magnetic fields on thermal convection. Instead of acting to stabilize convection through the modification of the Schwarzschild criterion, the method acts to reduce the efficiency of convection. Ultimately, the two approaches represent different physical mechanisms by which a star may produce its magnetic field.

A dynamo that sources its energy primarily from rotation will act to stabilize convection and will not drain the energy from convective elements. On the other hand, a turbulent dynamo will tend to exhaust the kinetic energy available from convection. The magnetic field created by a turbulent dynamo may also act to stabilize convection, but this effect is secondary in our models. The magnetic field strengths required to inflate a star following the turbulent dynamo approach are considerably weaker than those required when assuming a rotationally driven dynamo. Given the two different mechanisms that may be producing stellar magnetic fields, it is worth exploring whether or not the two approach produce any discernible differences between two otherwise identical stars. We have found the surface magnetic field strengths will be different, but is the stellar interior structure different between the two?

Figure 16 shows the run of density within three different model interiors: one standard, non-magnetic model and two magnetic models with different dynamo methods. Each model was computed with a mass of 0.599 $M_\odot$, a metallicity of −0.20 dex, and evolved to an age of 360 Myr—the properties of the YY Gem stars. The non-magnetic model has a radius smaller than the actual radius of the YY Gem (here considered a single star). Surface magnetic field strengths used in the magnetic models were those required to reconcile model radii with observations (4.3 kG and 0.7 kG for the Feiden & Chaboyer 2012b prescription and turbulent dynamo, respectively).

Overall, introducing a magnetic field causes the density profile to steepen within the models with little to no change in the central density. As can be seen in Figure 16, the magneto-convection methods produce identical results (the two lines are lying on top of one another) despite having different magnetic field strengths throughout. Only near the surface of the model (outer 0.2% by radius) do the two methods produce noticeable differences. We compared the sound speed profiles of the three models, as well, and found similar results. The two magnetic models were characterized by slower sound speed throughout compared to the standard model (as expected since they show lower densities). Differences between the two magnetic models were again noted in the outermost layers, where the sound speed of the turbulent dynamo model followed the sound speed of the non-magnetic model before deviating and tracking the rotational dynamo model throughout the rest of the model

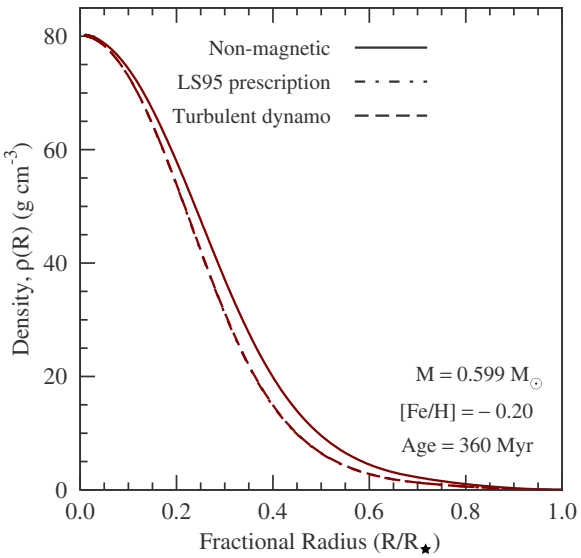

Figure 16. Interior density profile for a $M = 0.599\ M_\odot$ model with and without the presence of a magnetic field. The magnetic models were computed with a surface magnetic field strength strong enough to reconcile the model radius with the observed radius of YY Gem (4.3 kG and 0.7 kG for the Feiden & Chaboyer 2012b prescription and turbulent dynamo approach, respectively). Note that the two lines for the magnetic models directly on top of one another.

(A color version of this figure is available in the online journal.)

interior. Even if one could perform seismology on stars in this mass range, differences in the outermost layers would be unobservable. Thus, for all practical purposes, the two magnetic models produce identical results.

Finally, we confirmed that the radius to the convection zone boundary was equivalent in the magnetic models. In the non-magnetic model, the convection zone boundary was located at $R/R_\star = 0.671$, but it receded to $R/R_\star = 0.691$ and $R/R_\star = 0.690$ for the magnetic models. Therefore, it appears that the only way to differentiate between the two proposed methods is to measure a star's surface magnetic field strength.

5.2. Comparison to Previous Work

Similar methods for incorporating the effects of a magnetic field have been performed previously. These previous studies have separately looked at magnetic stabilization of convection (Mullan & MacDonald 2001) and the reduction of convective efficiency (Chabrier et al. 2007). It is instructive to compare the results presented in this paper with those earlier studies.

Qualitatively, our initial approach to modeling the magnetic interaction with convection (Feiden & Chaboyer 2012b) is very similar to the method favored by Mullan & MacDonald (2001). The variable ν, a "magnetic compression coefficient," appearing in our modified Schwarzschild criterion (Equation (53) in Feiden & Chaboyer 2012b) is essentially equal to the Mullan & MacDonald (2001) convective inhibition parameter, $\delta_{\rm MM}$. Explicitly,

$$\nu = -\left(\frac{\partial \ln \rho}{\partial \ln \chi}\right)_{P,\,T} = \frac{B^2}{B^2 + 8\pi P_{\rm gas}}. \tag{11}$$

Comparing with the magnetic inhibition parameter presented by Mullan & MacDonald (2001),

$$\delta_{\rm MM} = \frac{B^2}{B^2 + 4\pi\gamma P_{\rm gas}}, \tag{12}$$

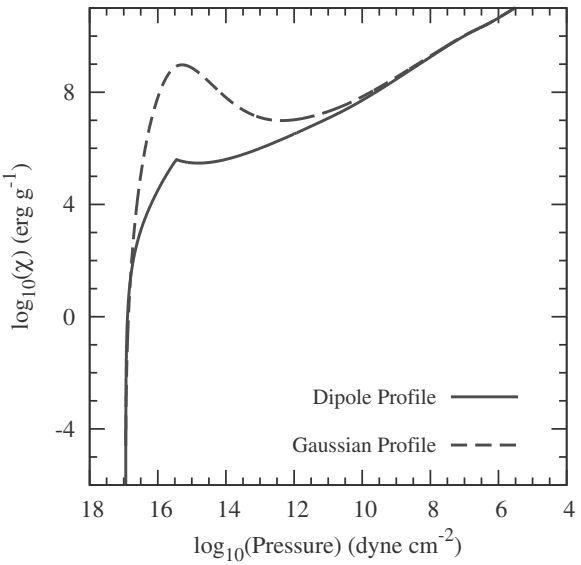

Figure 17. Variation of the magnetic energy per unit mass, χ, vs. the total pressure shown for two magnetic field radial profiles: dipole (solid line) and Gaussian (dashed line). A fixed mass ($M = 0.5\ M_{\odot}$) and surface magnetic field strength ($\langle Bf \rangle = 2.0$ kG) was used to generate each profile at a model age of 1 Gyr.

where γ, the ratio of specific heats, is of order unity. Their formulation is based on the work of Gough & Tayler (1966). One significant difference is that our approach introduces a magnetic energy gradient, ∇_{χ}, in the stability criterion. This gradient determines how the magnetic field, characterized by ν, interacts with convection. The ∇_{χ} term appears in our equations because we allow the magnetic pressure gradient to influence the equilibrium density (Equation (34) in Feiden & Chaboyer 2012b). Gough & Tayler (1966) restricted themselves to simple field geometries in a medium with uniform density. It is for this reason that we favor our approach and the inclusion of ∇_{χ} in the stability criterion.

Figure 17 shows how the magnetic energy varies as a function of pressure for our two radial profiles. Immediately it can be seen that the two profiles differ significantly near the base of the convection zone around $\log_{10}(P) \sim 15.5$. Throughout a large portion of the convection zone, the gradient is dominated not by the magnetic field radial profile, but by the density profile. Density increases steeply with radius in the outer regions of the star. Since $\chi\ (= B^2/8\pi\rho)$ is inversely proportional to density, we see a decrease in χ in the outer layers. A negative gradient in Figure 17 implies that the magnetic field has a stabilizing effect on convection. Since the gradient in density dominates, the effect of magneto-convection is rather independent of the radial profile (so long as the magnetic field is an increasing function of depth from the surface).

Deeper in the star, where the two radial profiles begin to deviate, we see that there is a change in slope for the Gaussian profile. In this region, the magnetic field strength gradient begins to dominate. Since the dipole profile has a shallower slope through the interior the change in slope occurs deeper in the star. A positive magnetic energy gradient in Figure 17 has a destabilizing effect on convection—convection becomes more favorable. However, since this change in slope occurs within an already convectively unstable region, the overall effect on stellar structure is minimal. One may then postulate that the dipole profile, with its almost continuous negative magnetic energy gradient should induce larger changes on stellar structure. But to maintain a negative slope the magnetic field strength cannot rise too rapidly, meaning the value of ν remains small.

Given our model's dependence on ∇_{χ} in the stability criterion, we expect our required magnetic field strengths to be about a factor of 2–5 larger than those required by Mullan & MacDonald (2001). Subsequent works incorporating the Mullan & MacDonald (2001) magnetic inhibition parameter do not explicitly model any of the three systems we have presented (e.g., MacDonald & Mullan 2010, 2012, 2013). However, drawing from the general conclusions of those works, it appears that they regularly require surface magnetic field strengths of about 0.5 kG to produce models consistent with observations. This is approximately an order of magnitude less than what we have presented in Section 3 using our original method (Feiden & Chaboyer 2012b). Only part of this difference can be accounted for by our inclusion of ∇_{χ} in the stability criterion. The rest of the difference may result from our incorporation of the magnetic field in the density equation of state. Additional tests must be carried out to assess the various contributions to these differences.

The tactic used in Section 4.4.3 has attempted to quantify a reduction in convective efficiency. Chabrier et al. (2007) had previously explored this concept, although they did so by arbitrarily reducing $\alpha_{\rm MLT}$. Although reducing $\alpha_{\rm MLT}$ can be considered conceptually different from our approach in Section 4.4.3, the two are remarkably similar.

Convective efficiency can be defined using the framework of MLT by considering heat losses that are "horizontal" to the radial motion of a bubble (Böhm-Vitense 1958; Weiss et al. 2004). The efficiency, Γ, can be expressed as

$$\Gamma = \frac{c_P}{6ac} \frac{\kappa \rho^2 u_{\rm conv} \alpha_{\rm MLT} H_P}{T^3}, \tag{13}$$

where c_P is the specific heat at constant pressure, a is the radiation constant, c is the speed of light in a vacuum, and κ is the opacity. Since the convective efficiency is proportional to both $u_{\rm conv}$ and $\alpha_{\rm MLT}$, we may compare reductions in $u_{\rm conv}$ with the reductions in $\alpha_{\rm MLT}$ used by Chabrier et al. (2007).

Consider a reduction in $u_{\rm conv}$ caused by a magnetic field that has a strength that is some fraction, Λ, of the equipartition field strength, $B_{\rm eq} = (4\pi\rho u_{\rm conv}^2)^{1/2}$. Then the ratio of the convective efficiency in the presence of a magnetic field to the non-magnetic efficiency is $\Gamma_{\rm mag}/\Gamma_0 = (1 - \Lambda^2)^{1/2}$. Therefore, to achieve the same results by reducing $\alpha_{\rm MLT}$, we need only multiply the solar $\alpha_{\rm MLT}$ by $(1 - \Lambda^2)^{1/2}$. We then find that

$$\Lambda = \left[1 - \left(\frac{\alpha_{\rm MLT}}{\alpha_{\rm MLT,\,\odot}} \right)^2 \right]^{1/2}. \tag{14}$$

This assumes that the convective velocity is unaffected by changes in mixing length. Allowing for changes in convective velocity, the exponent on the mixing length term in Equation (14) can be larger. We now have a quantitative description of the degeneracy between magnetic inhibition of convection and reducing the convective mixing length (Cox et al. 1981; MacDonald & Mullan 2010) in terms of a fraction of the equipartition magnetic field strength.

Chabrier et al. (2007) considered multiple values for $\alpha_{\rm MLT}$, including $\alpha_{\rm MLT} = 0.1$ and $\alpha_{\rm MLT} = 0.5$. These drastically reduced $\alpha_{\rm MLT}$ values correspond to $\Lambda \sim 0.999$ and $\Lambda \sim 0.966$, respectively. We find that our models do require such strong magnetic fields, at least in the outer layers. The model of YY

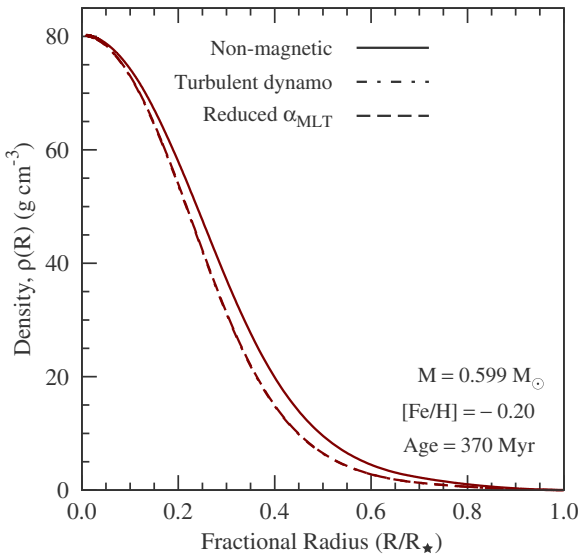

Figure 18. Similar to Figure 16, but comparing a reduced α_{MLT} model with a turbulent dynamo magnetic model. The turbulent dynamo model has a 0.7 kG surface magnetic field and the reduced α_{MLT} model has $\alpha_{MLT} = 0.6$. Note that the magnetic model and reduced α_{MLT} model profiles lie on top of one another. (A color version of this figure is available in the online journal.)

Gem in Section 4.4.3 has $\Lambda \sim 1$ throughout a large portion of the outer envelope. Λ decreases from 1 at the photosphere (where $T = T_{\rm eff}$) to 0.3 at the point where we match the envelope to the interior. This is the result of prescribing a magnetic field radial profile that is independent of Λ.

To make the comparison more direct, we compare the interior structure of the magnetic model with that from a reduced α_{MLT} model. Our models required $\alpha_{MLT} = 0.60$ to reproduce the observed radius of YY Gem, corresponding to $\Lambda = 0.951$, for reference. Based on Figure 1(a) of Chabrier et al. (2007) it appears that they require $\alpha_{MLT} \sim 0.4$ to reproduce the properties of YY Gem. We compare the density distribution of our reduced α_{MLT} and magnetic model in Figure 18. We find no significant difference. It is apparent that our magnetic model produces results consistent with reduced α_{MLT} models.

5.3. Star Spots

Up to this point we have avoided any mention of specifically incorporating effects due to star spots. Previous magnetic investigations have accounted for dark spots by reducing the total flux at the model photosphere (Spruit & Weiss 1986; Chabrier et al. 2007; Morales et al. 2010; MacDonald & Mullan 2012, 2013). Reductions of photospheric flux were combined with the aforementioned magneto-convection techniques to reconcile model radii with observations of DEBs (Chabrier et al. 2007; MacDonald & Mullan 2012). However, as we have shown, our models do not explicitly require spots to produce agreement with observations.

This can be understood by considering that there is a degeneracy between effects due to spots and effects due to magneto-convection (MacDonald & Mullan 2010). Generally, the total flux leaving the model photosphere is reduced. By including spots, magnetic field strengths required by the models to reproduce observations would be decreased. We elected to not include spots explicitly for two reasons: (1) spots are the manifestation of inhibited, or suppressed, convection, and (2) average surface magnetic field strengths are more easily measured than spot properties.

Spots are surface blemishes caused by a reduction in convective energy transport. Therefore, we are of the opinion that modeling effects of magnetic fields on convection is a more direct way to model effects from spots. Convective properties required by our models represent the average global properties of convection, producing a convective flux that is between the increased convective flux in unspotted areas and the reduced convective flux below spots.

Possibly of greater importance, however, is that surface magnetic field strengths are directly observable. If effects of spots on stellar structure are distinct from magneto-convection formulations, differences should appear between measured surface magnetic field strengths and those required by stellar models. The problem with immediately including spots is that required spot properties are difficult to validate, especially for M-dwarfs. Including spots in stellar models requires the specification of a free parameter that describes a surface coverage of black ($T = 0$ K) spots equivalent to a desired surface coverage of gray ($T > 0$ K) spots (Spruit & Weiss 1986). Measuring either the effective coverage of black spots or the actual coverage of gray spots on real stars is a highly uncertain process. Therefore, it may be better to probe whether spots must be considered independently from magneto-convection by comparing pure magneto-convection models to magnetic field observations to look for discrepancies between surface magnetic field strengths.

5.4. Implications for Asteroseismology

Figure 16 showed that magnetic models have a lower density throughout their interior than do non-magnetic models. This is not unexpected if we consider that the magnetic field acts to inflate the radius of the model. However, the reduction in mass density throughout the stellar interior affects the sound speed profile, which has implications for seismic analyses.

We plot the sound speed profile for two $M = 0.6\,M_\odot$ models in Figure 19. The sound speed is defined as

$$c_s^2 = \frac{P}{\rho}\left(\frac{\partial \ln P}{\partial \ln \rho}\right)_{\rm ad} \tag{15}$$

where P is the total pressure (gas + radiation + magnetic) and ρ is the mass density. Using the total pressure to define the sound speed will suffice for exploratory purposes. The models have a scaled-solar composition of [Fe/H] $= -0.2$ dex. One model has a magnetic field with a surface field strength of 0.7 kG using the turbulent dynamo formulation. Note that the density profile for these two models are shown in Figure 16.

Comparing the sound speed between the two models, we see that the magnetic model has a sound speed that is slower by about 5%. The bottom panel in Figure 19 shows the relative sound speed difference between the two models with respect to the non-magnetic models. We define

$$\frac{\delta c_s}{c_s} = \frac{c_{s,\,\rm mag} - c_{s,\,0}}{c_{s,\,0}}, \tag{16}$$

where $c_{s,\,0}$ is the sound speed in the non-magnetic model and $c_{s,\,\rm mag}$ is that for the magnetic model. The change in sound speed between the two models affects the p-mode frequencies and frequency spacing, which consequently alters the interpretation of seismic data.

Imagine that observational data is obtained for a $M = 0.6\,M_\odot$ star that has a 0.7 kG magnetic field. These two facts about the star are unknown to the observer. Instead, the observer has taken

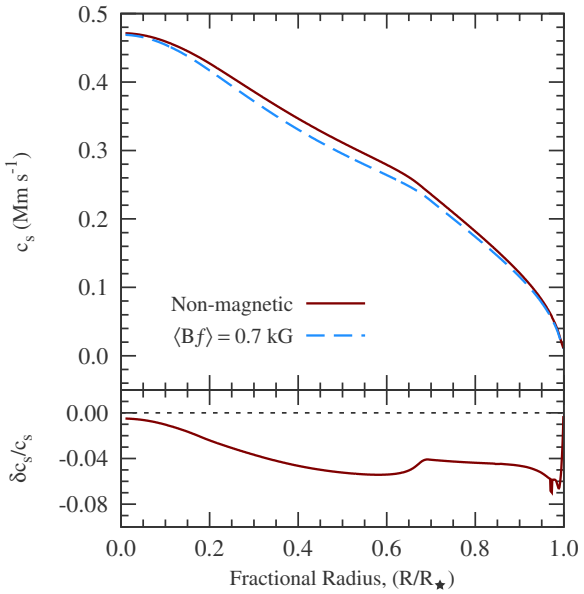

Figure 19. Top: sound speed profile for a $M = 0.599\,M_{\odot}$ model with and without the presence of a magnetic field. Bottom: relative difference in the sound speed profile between the two models with respect to the non-magnetic model. The magnetic model was computed with a surface magnetic field strength strong enough to reconcile the model radius with the observed radius of YY Gem (0.7 kG).

(A color version of this figure is available in the online journal.)

great care to obtain high resolution spectra with sufficiently high signal-to-noise. From this data they are able to ascertain the effective temperature, $T_{\rm eff}$, and the approximate composition. They also have precise photometric data that allows for a seismic analysis. To first order, they are able to obtain the stellar radius from the large frequency splittings. The properties they derive for the star are $R = 0.619 \pm 0.006\ R_{\odot}$, $T_{\rm eff} = 3\,820 \pm 100$ K, and $[{\rm Fe/H}] = -0.2 \pm 0.1$.[9]

With these properties, what inferences would the observer make about the star? Using a grid of non-magnetic Dartmouth models (Dotter et al. 2008; Feiden & Chaboyer 2012a) the observer would estimate the mass of the star to be roughly $M = 0.67 \pm 0.02\,M_{\odot}$. Or approximately 10% larger than the actual mass. The age of the star would be difficult to estimate in this particular case due to the lack of significant radius evolution of low-mass stars on the MS. One concession, is that the models would not match the observed $T_{\rm eff}$ within the 1σ limit quoted above. However, one can easily find a match within 2σ. Moreover, the sound speed profiles between the higher mass non-magnetic models and the lower mass magnetic models are quite similar.

As we have seen in Section 3.2, given a radius, $T_{\rm eff}$, and metallicity, one should be able to derive the appropriate mass for this star. With magnetic models, a slight degeneracy in mass and magnetic field strength would be introduced, as varying the magnetic field at a given mass can alter the radius and $T_{\rm eff}$. However, the true solution would be encompassed by the formal uncertainties. Regardless, it will be more accurate than if only non-magnetic models were used.

Future investigations exploring the effects of a magnetic perturbation on the pulsation analysis and the use of magnetic models for mass determinations are warranted. While the case above was exploratory and does not represent the typical stars selected for asteroseismic analysis, the conclusions should be valid for all stars with an outer convective envelope. Magnetically active stars are also not favored for asteroseismology. There are issues with removing possible photometric variations due to spots. However, the lack of photometric variability from spots is not necessarily indicative of an inactive star (Jackson & Jeffries 2013).

[9] Conveniently, these are the properties of YY Gem.

5.5. Exoplanet Properties

The primary effect of introducing a magnetic perturbation is that model radii are increased and $T_{\rm eff}$ are decreased. What has not been discussed is that model luminosities show a marginal decrease. This means the radius increase does not precisely balance the cooling of the $T_{\rm eff}$, in contrast with what has been assumed previously (see, e.g., Morales et al. 2008). While there is no luminosity change immediately after the perturbation is introduced, the reduction in luminosity occurs over thermal timescales. The models readjust their internal structure to compensate for the reduction of convective heat flux. These changes in the stellar surface properties can influence studies of extra-solar planets (exoplanets) around low-mass stars.

Transiting exoplanets have radii that are directly proportional to the radii of their host stars (e.g., Seager & Mallén-Ornelas 2003). Determining the radius of a low-mass host star is difficult. Interferometry allows for the direct measurement of the stellar radius, but is only available for the brightest (i.e., nearest) targets (von Braun et al. 2012; Boyajian et al. 2012). One could attempt to perform an asteroseismic analysis, but it would suffer due to the intrinsic faintness of low-mass stars and also from the considerable photometric variability that is characteristic of these stars. In lieu of other methods, stellar evolution models are often used to aid in the interpretation of transiting exoplanetary systems (e.g., Muirhead et al. 2012; Gaidos 2013; Dressing & Charbonneau 2013).

Owing to a lack of available magnetic model grids, these studies have relied exclusively on standard stellar evolution models. The use of magnetic models can have an impact on these studies. For instance, Muirhead et al. (2012) measured the metallicity and $T_{\rm eff}$ for the low-mass stars tagged as planet candidates in the *Kepler* mission (Batalha et al. 2013). They then interpolated within Dartmouth isochrones (Dotter et al. 2008) to determine stellar radii. Had they used magnetic stellar models, for a given $T_{\rm eff}$, the stellar radius would be larger, with the precise factor dependent on the magnetic field strength assumed. This would result in larger, less dense (and therefore less Earth-like) planets.

Estimating the surface magnetic field is the largest hindrance to using magnetic models. Stars in the *Kepler* field are typically distant, meaning X-ray measurements will not necessarily be available. Deep observations of the *Kepler* field with *Chandra* or *XMM-Newton* could provide X-ray magnetic activity information. Alternatively, it might be feasible to obtain optical spectra and use the Hα equivalent widths to estimate magnetic activity. Hα is less revealing, as we are not aware of a direct relation linking Hα equivalent widths to magnetic field strengths. However, it has been shown that Hα equivalent widths correlate, to some extent, with X-ray luminosity (Delfosse et al. 1998; Reiners & Basri 2007; Stassun et al. 2012). Regardless, the presence of Hα in emission would be indicative of an active star. At that point, several magnetic models could be used to constrain the stellar radius.

6. CONCLUSIONS

This paper addressed the question of how the presence of a magnetic field affects the structure of low-mass stars with a radiative core. We approached this problem by taking a careful look at three DEB systems that show significant radius and $T_{\rm eff}$ deviations from standard stellar evolution models. Using the magnetic stellar evolution models introduced in a previous paper (Feiden & Chaboyer 2012b), we attempted to reproduce the observational properties of UV Psc, YY Gem, and CU Cnc.

After finding that the magnetic models were able to reconcile the stellar models with the observed radii and $T_{\rm eff}$s (consistent with the findings of Mullan & MacDonald 2001), it was shown in Section 4.2 that the surface magnetic field strengths were likely too strong. This was determined by taking the coronal X-ray luminosity as an indirect diagnostic for the surface magnetic field strength (Fisher et al. 1998; Pevtsov et al. 2003). In contrast to the surface magnetic fields, the interior field strengths are of a plausible magnitude, consistent with the range of field strengths predicted to be within the Sun by 3D MHD models (Brandenburg & Subramanian 2005).

We then attempted to reduce the surface magnetic field strengths while still maintaining the newfound agreement between stellar models and DEB observations. The most plausible explanation we uncovered is that kinetic energy in turbulent convective flows is actively converted into magnetic energy. Introducing changes to MLT that mimic this physical process yielded accurate models with surface magnetic field strengths nearly equal to those predicted by X-ray emission. We were unable, however, to implement this prescription for the stars of UV Psc. This is likely a consequence of the chosen magnetic field profile, which caused the models to fail to converge. We note that by invoking the "turbulent dynamo" approach, we are able to generate substantial radius inflation with relatively modest (sub-kG) magnetic fields.

Beyond direct comparisons to observational data, we explored additional implications of the present study. We found that different theoretical descriptions of the physical manifestation of magneto-convection lead to similarly inflated stars and produce nearly identical stellar interiors. This was evidence by the radial density profile for models invoking the methods presented in Feiden & Chaboyer (2012b), Section 4.4.3 (this work), and Chabrier et al. (2007), which were all nearly identical. The latter uses a reduced MLT approach to simulate the introduction of a turbulent dynamo. We provide a variable, Λ, to translate a reduction in mixing length into a magnetic field strength (normalized to the equipartition field strength, which depends on the convective velocity).

We also argue that asteroseismic studies should be relatively unaffected by structural changes in the stellar models. Asteroseismic studies typically know the stellar composition and effective temperature. Anomalous values of the $T_{\rm eff}$ due to magnetic fields should provide a clue that magnetic fields are required. For a given density profile, it is difficult to reproduce the $T_{\rm eff}$ for a star of a given mass without a magnetic field. If this happens, it might be a hint to adopt magnetic models. Otherwise, if the $T_{\rm eff}$ is ignored, then masses would typically be overestimated by about 10%.

Magnetic models will, however, have an immediate impact on the estimated radii of transiting exoplanets. The radii of transiting exoplanetary radii scale with the stellar radius. This is but one reason that further exploration of the role of magnetic fields in low-mass stars is required. Interpretation of low-mass star observations depend critically on the accuracy of stellar evolution model predictions.

G.A.F. thanks A. Brandenburg for the discussions that lead to the development of the turbulent dynamo models advanced in this paper. The authors thank the anonymous referee whose comments, questions, and suggestions improved the manuscript. The authors also thank the William H. Neukom 1964 Institute for Computational Science at Dartmouth College and the National Science Foundation (NSF) grant AST-0908345 for their support. This research has made use of NASA's Astrophysics Data System, the SIMBAD database, operated at CDS, Strasbourg, France, and the *ROSAT* data archive tools hosted by the High Energy Astrophysics Science Archive Research Center (HEASARC) at NASA's Goddard Space Flight Center.

APPENDIX

MAGNETIC FLUX SCALING RELATION

We compute the approximate unsigned surface magnetic flux for the dwarf stars presented in the Reiners (2012) review. The data are compiled in Table 6. Reiners (2012) collected all of the reliably determined magnetic field measurements for cool dwarf stars. We select for our sample only those stars that had their average surface magnetic field, $\langle Bf \rangle$, measured using Stokes I polarization observations. We avoided using stars with estimates provided from Stokes V observations because Stokes I yields a more accurate estimate of $\langle Bf \rangle$ (Reiners & Basri 2009). Since our models predict $\langle Bf \rangle$, Stokes I observations give a more direct comparison.

We cross-correlated objects from Reiners (2012) with the *ROSAT* Bright and Faint Source Catalogues (Voges et al. 1999, 2000) to extract X-ray count rates ($X_{\rm cr}$) and HRs. Objects that did not have an X-ray counterpart were excluded from our final sample. We identified all of the stars in the remaining subset that had parallax estimates from *Hipparcos* (van Leeuwen 2007). Our final sample consists of 25 objects with both X-ray counterparts and parallax measurements. Two additional data points for G-dwarfs, not found in Reiners (2012), were included (Anderson et al. 2010) bringing the total number of objects to 27. Conversion from raw $X_{\rm cr}$, HR, and parallaxes to X-ray luminosities is described in Section 4.2. The full sample of objects, their magnetic field properties, and X-ray properties are given in Table 6.

Results of extending the scaling relation with our sample are presented in Figure 10. The data used by Pevtsov et al. (2003) is shown for reference. Our data follows the same trend, but is more populated at the low L_x end. We caution that the data presented in Figure 10 suffer from uncertainty in the adopted stellar radii. When possible, we adopted the radii quoted by the original sources, although their procedure for assigning radii was not always clear. For stars where the original references did not have quoted radii, we assigned radii based on spectral type using interferometric data as a guide (Boyajian et al. 2012). Using spectral types as an indicator for stellar properties is hazardous, especially for M-dwarfs, but we assumed large radius uncertainties that would likely encompass the true value.

The data are also limited by the spatial resolution of *ROSAT*. As an example, CV Cnc is an mid-M-dwarf binary included in our final data set. Estimates of its X-ray luminosity include contributions from CU Cnc, as discussed in Section 3.3. Only for CV Cnc did we correct for this confusion. Overall, uncertainty

Table 6
Low-mass Stars from Reiners (2012) with Direct Magnetic Field Measurements Used to Derive our $\Phi - L_x$ Relation

Star Name	Other Name	SpT	$\langle Bf \rangle$ (kG)	$R_\star$ ($R_\odot$)	log(Φ) (Mx)	π (mas)	X_{cr} (counts s^{-1})	HR	log(F_x) (erg s^{-1} cm^{-2})	log(L_x) (erg s^{-1})
HD 115383	59 Vir	G0	0.5	0.74	25.22	56.95	1.12	−0.14	−11.07	29.50
HD 115617	61 Vir	G6	0.1	0.95	24.74	116.89	0.01	−0.96	−13.34	26.60
σ Dra	...	K0	0.1	0.80	24.59	173.77	0.26	−0.80	−11.97	27.62
40 Eri	...	K1	0.1	0.75	24.53	200.62	0.80	−0.28	−11.26	28.21
ϵ Eri	...	K2	0.1	0.70	24.59	310.94	2.82	−0.44	−10.77	28.32
LQ Hya	...	K2	2.5	0.70	25.86	53.70	2.73	−0.04	−10.66	29.96
GJ 566 B	ξ Boo B	K4	0.5	0.70	25.14	149.26	2.44	−0.31	−10.79	28.94
Gl 171.2 A	...	K5	1.4	0.65	25.56	55.66	2.69	−0.04	−10.66	29.93
Gl 182	...	M0.0	2.5	0.60	25.74	38.64	0.65	−0.19	−11.32	29.58
Gl 803	AU Mic	M1.0	2.3	0.50	25.54	100.91	5.95	−0.07	−10.33	29.74
Gl 569 A	...	M2.0	1.8	0.40	25.24	...	0.49	−0.40	−11.52	...
Gl 494	DT Vir	M2.0	1.5	0.40	25.16	85.54	1.57	−0.01	−10.89	29.33
Gl 70	...	M2.0	0.2	0.33	24.12	87.62	0.04	−0.67	−12.68	27.51
Gl 873	EV Lac	M3.5	3.8	0.31	25.35	195.22	5.83	−0.16	−10.36	29.14
Gl 729	V1216 Sgr	M3.5	2.1	0.20	24.71	336.72	0.94	−0.43	−11.25	27.78
Gl 87	...	M3.5	3.9	0.30	25.33	96.02	...	...	...	...
Gl 388	AD Leo	M3.5	3.0	0.39	25.44	213.00	3.70	−0.27	−10.59	28.83
GJ 3379	...	M3.5	2.3	0.25	24.94	190.93	0.40	−0.20	−11.54	27.98
GJ 2069 B	CV Cnc	M4.0	2.7	0.25	25.01	78.10	0.24	−0.14	−11.74	27.95
Gl 876	IL Aqr	M4.0	0.2	0.31	24.07	213.28	...	...	...	...
GJ 1005 A	...	M4.0	0.2	0.23	23.81	191.86	...	...	...	...
Gl 490 B	G 164-31	M4.0	3.2	0.20	24.89	50.00	0.84	−0.22	−11.22	29.46
Gl 493.1	FN Vir	M4.5	2.1	0.20	24.71	123.10	0.14	−0.16	−11.98	27.92
GJ 4053	LHS 3376	M4.5	2.0	0.17	24.55	137.30	0.06	−0.49	−12.46	27.34
GJ 299	...	M4.5	0.5	0.18	23.99	148.00	...	...	...	...
GJ 1227	...	M4.5	0.2	0.19	23.64	120.00	...	...	...	...
GJ 1224	...	M4.5	2.7	0.18	24.73	132.60	0.21	−0.45	−11.91	27.93
Gl 285	YZ Cmi	M4.5	4.5	0.30	25.39	167.88	1.47	−0.21	−10.97	28.65
GJ 1154 A	...	M5.0	2.1	0.20	24.71	...	0.10	−0.23	−12.15	...
GJ 1156	GL Vir	M5.0	2.1	0.16	24.51	152.90	0.13	−0.25	−12.04	27.67
Gl 905	HH And	M5.5	0.1	0.17	23.24	316.70	0.18	0.15	−11.79	27.29
GJ 1057	CD Cet	M5.5	0.1	0.18	23.29	117.10	...	...	...	...
GJ 1245 B	...	M5.5	1.7	0.14	24.31	220.00	0.20	−0.37	−11.90	27.50
GJ 1286	...	M5.5	0.4	0.14	23.68	138.30	...	...	...	...
GJ 1002	...	M5.5	0.2	0.13	23.31	213.00	...	...	...	...
Gl 406	CN Leo	M5.5	2.4	0.13	24.39	418.30	0.23	−0.22	−11.79	27.05
Gl 412 B	WX Uma	M6.0	3.9	0.13	24.60	206.94	0.18	−0.64	−12.05	27.39
GJ 1111	DX Cnc	M6.0	1.7	0.12	24.17	275.80	...	...	...	...
Gl 644C	VB 8	M7.0	2.3	0.10	24.15	153.96	...	...	...	...
GJ 3877	LHS 3003	M7.0	1.5	0.10	23.96	157.80	...	...	...	...
GJ 3622	...	M7.0	0.6	0.10	23.56	221.00	...	...	...	...
LHS 2645	...	M7.5	2.1	0.08	23.91	...	...	...	...	...
LP 412-31	...	M8.0	3.9	0.08	24.18	...	...	...	...	...
VB 10	V1298 Aql	M8.0	1.3	0.08	23.70	164.30	...	...	...	...
LHS 2924	...	M9.0	1.6	0.08	23.79	90.00	...	...	...	...
LHS 2065	...	M9.0	3.9	0.08	24.18	116.80	...	...	...	...

in the stellar radius affects the magnetic flux while the lack of spatial resolution affects the X-ray luminosity. Therefore, we believe our estimates are robust, particularly given that Figure 10 is plotted using logarithmic units, where a factor of two does not contribute to a significant shift in the data.

The regression line and associated uncertainty limits shown in Figure 10 were obtained by performing an ordinary least squares (OLS) regression. A standard OLS was selected as we are not attempting to establish a causal relationship between Φ and L_x (Isobe et al. 1990). Our primary concern is developing a relationship that permits a prediction of Φ given a value for L_x. Following the recommendations of Isobe et al. (1990) and Feigelson & Babu (1992), we perform an OLS($\log_{10}\Phi|\log_{10} L_x$), where $\log_{10} L_x$ is the predictor variable and $\log_{10}\Phi$ is the variable to be predicted. Note that we transformed the variables to a logarithmic scale because the data extends over several orders of magnitude in Φ and L_x.

The result of the OLS analysis yielded a regression line

$$\log_{10}\Phi = (24.873 \pm 0.004) + (0.459 \pm 0.018) \times (\log_{10} L_x - \mu_x), \quad \text{(A1)}$$

where μ_x is the mean value of $\log_{10} L_x$ taken over the entire sample. A shift of the dependent variable was performed prior to the regression analysis. By doing this, we were able to minimize the error associated with the y-intercept. However, the standard deviation of the mean, σ_x, becomes the largest source of error.

We found $\mu_x = 28.34 \pm 0.97$, where we took

$$\sigma_x = \sqrt{\frac{1}{N-1}\sum_{i=1}^{N}(x_i - \mu_x)^2}. \quad \text{(A2)}$$

We opted for computing the standard deviation with $N - 1$ because of our small sample (27 data points) so as to provide a conservative error estimate.

REFERENCES

Adams, W. S., & Joy, A. H. 1920, PASP, 32, 276
Adelberger, E. G., García, A., Robertson, R. G. H., et al. 2011, RvMP, 83, 195
Agrawal, P. C., Riegler, G. R., & Garmire, G. P. 1980, MNRAS, 192, 725
Andersen, J. 1991, A&ARv, 3, 91
Anderson, R. I., Reiners, A., & Solanki, S. K. 2010, A&A, 522, A81
Anosova, Z. P., Orlov, V. V., & Chernyshev, M. V. 1989, SvAL, 15, 3
Antia, H. M., Chitre, S. M., & Thompson, M. J. 2000, A&A, 360, 335
Antia, H. M., Chitre, S. M., & Thompson, M. J. 2003, A&A, 399, 329
Antonopoulou, E. 1987, Ap&SS, 135, 335
Bahcall, J. N., Serenelli, A. M., & Basu, S. 2005, ApJ, 621, L85
Baraffe, I., Chabrier, G., Allard, F., & Hauschildt, P. H. 1998, A&A, 412, 403
Barden, S. C. 1985, ApJ, 295, 162
Barrado y Navascués, D., Fernández-Figueroa, M. J., García-López, R. J., De Castro, E., & Cornide, M. 1997, A&A, 326, 780
Basu, S. 1998, MNRAS, 298, 719
Basu, S., & Antia, H. M. 1997, MNRAS, 287, 189
Basu, S., & Antia, H. M. 2004, ApJL, 606, L85
Batalha, N. M., Rowe, J. F., Bryson, S. T., et al. 2013, ApJS, 204, 24
Bender, C. F., Mahadevan, S., Deshpande, R., et al. 2012, ApJ, 751, L31
Böhm-Vitense, E. 1958, ZAp, 46, 108
Bonaca, A., Tanner, J. D., Basu, S., et al. 2012, ApJL, 755, L12
Boyajian, T. S., von Braun, K., van Belle, G., et al. 2012, ApJ, 757, 112
Brandenburg, A., & Subramanian, K. 2005, PhR, 417, 1
Brown, B. P., Browning, M. K., Brun, A. S., Miesch, M. S., & Toomre, J. 2010, ApJ, 711, 424
Çakırlı, Ö., İbanoğlu, C., & Dervisoglu, A. 2010, RMxAA, 46, 363
Çakırlı, Ö., Ibanoglu, C., & Sipahi, E. 2013a, NewA, 20, 1
Caillault, J.-P. 1982, AJ, 87, 558
Çakırlı, Ö., İbanoğlu, C., & Sipahi, E. 2013b, MNRAS, 429, 85
Carr, R. B. 1967, AJ, 72, 788
Casagrande, L., Flynn, C., Portinari, L., Girardi, L., & Jimenez, R. 2007, MNRAS, 382, 1516
Chabrier, G., & Baraffe, I. 1995, ApJ, 451, L29
Chabrier, G., Gallardo, J., & Baraffe, I. 2007, A&A, 472, L17
Chabrier, G., & Küker, M. 2006, A&A, 446, 1027
Charbonneau, D. 2009, in IAU Symp. 253, Transiting Planets, ed. F. Pont, D. Sasselov, & M. Holman (Cambridge: Cambridge Univ. Press), 1
Cox, A. N., Hodson, S. W., & Shaviv, G. 1981, ApJL, 245, L37
Cutri, R. M., Skrutskie, M. F., van Dyk, S., et al. 2003, yCat, 2246, 0
Delfosse, X., Forveille, T., Mayor, M., Burnet, M., & Perrier, C. 1999, A&A, 341, L63
Delfosse, X., Forveille, T., Perrier, C., & Mayor, M. 1998, A&A, 331, 581
Dobler, W., Stix, M., & Brandenburg, A. 2006, ApJ, 638, 336
Donati, J.-F., & Landstreet, J. D. 2009, ARA&A, 47, 333
Dotter, A., Chaboyer, B., Jevremović, D., et al. 2007, AJ, 134, 376
Dotter, A., Chaboyer, B., Jevremović, D., et al. 2008, ApJS, 178, 89
Doyle, J. G., Butler, C. J., van den Oord, G. H. J., & Kiang, T. 1990, A&A, 232, 83
Doyle, J. G., & Mathioudakis, M. 1990, A&A, 227, 130
Doyle, L. R., Carter, J. A., Fabrycky, D. C., et al. 2011, Sci, 333, 1602
Dressing, C. D., & Charbonneau, D. 2013, ApJ, 767, 95
Durney, B. R., De Young, D. S., & Roxburgh, I. W. 1993, SoPh, 145, 207
Feiden, G. A. 2013, PhD thesis, Dartmouth College (Hanover, NH)
Feiden, G. A., & Chaboyer, B. 2012a, ApJ, 757, 42
Feiden, G. A., & Chaboyer, B. 2012b, ApJ, 761, 30
Feiden, G. A., Chaboyer, B., & Dotter, A. 2011, ApJL, 740, L25
Feigelson, E. D., & Babu, G. J. 1992, ApJ, 397, 55
Fisher, G. H., Longcope, D. W., Metcalf, T. R., & Pevtsov, A. A. 1998, ApJ, 508, 885
Fuchs, B., Dettbarn, C., Rix, H.-W., et al. 2009, AJ, 137, 4149
Gaidos, E. 2013, ApJ, 770, 90
Gillon, M., Bonfils, X., Demory, B.-O., et al. 2010, A&A, 525, A32
Gough, D. O., & Tayler, R. J. 1966, MNRAS, 133, 85
Grevesse, N., & Noels, A. 1993, in Origin and Evolution of the Elements, ed. N. Prantzos, E. Vangioni-Flam, & M. Casse (Cambridge: Cambridge Univ. Press), 15
Grevesse, N., & Sauval, A. J. 1998, SSRv, 85, 161
Güdel, M., Audard, M., Magee, H., et al. 2001, A&A, 365, L344
Güdel, M., Schmitt, J. H. M. M., Bookbinder, J. A., & Fleming, T. A. 1993, ApJ, 415, 236
Haro, G., Chavira, E., & Gonzalez, G. 1975, IBVS, 1031, 1
Henyey, L. G., Vardya, M. S., & Bodenheimer, P. 1965, ApJ, 142, 841
Hoxie, D. T. 1970, ApJ, 161, 1083
Hoxie, D. T. 1973, A&A, 26, 437
Hussain, G. A. J., Brickhouse, N. S., Dupree, A. K., et al. 2012, MNRAS, 423, 493
Hut, P. 1981, A&A, 99, 126
Ibanoglu, C. 1987, Ap&SS, 139, 139
Irwin, J. M., Quinn, S. N., Berta, Z. K., et al. 2011, ApJ, 742, 123
Isobe, T., Feigelson, E. D., Akritas, M. G., & Babu, G. J. 1990, ApJ, 364, 104
Jackson, R. J., & Jeffries, R. D. 2013, MNRAS, 431, 1883
Johns-Krull, C. M. 2007, ApJ, 664, 975
Joy, A. H., & Sanford, R. F. 1926, ApJ, 64, 250
Kjurkchieva, D. P., Marchev, D. V., Heckert, P. A., & Ordway, J. I. 2005, AJ, 129, 1084
Kraus, A. L., Tucker, R. A., Thompson, M. I., Craine, E. R., & Hillenbrand, L. A. 2011, ApJ, 728, 48
Kron, G. E. 1952, ApJ, 115, 301
Lastennet, E., Fernandes, J., & Oblak, E. 2003, A&A, 409, 611
Laughlin, G., Bodenheimer, P., & Adams, F. C. 1997, ApJ, 482, 420
Leung, K.-C., & Schneider, D. P. 1978, AJ, 83, 618
Limber, D. N. 1958, ApJ, 127, 363
Liu, Q., Yang, Y., Gu, S., & Hang, Z. 1996, IBVS, 4326, 1
López-Morales, M. 2007, ApJ, 660, 732
Lydon, T. J., & Sofia, S. 1995, ApJ, 101, 357
MacDonald, J., & Mullan, D. J. 2010, ApJ, 723, 1599
MacDonald, J., & Mullan, D. J. 2012, MNRAS, 421, 3084
MacDonald, J., & Mullan, D. J. 2013, ApJ, 765, 126
Mahadevan, S., Ramsey, L., Bender, C., et al. 2012, Proc. SPIE, 8446, 84461S
Mamajek, E. E., Bartlett, J. L., Seifahrt, A., et al. 2013, AJ, 146, 154
McLean, M., Berger, E., & Reiners, A. 2012, ApJ, 746, 23
Montes, D., de Castro, E., Fernandez-Figueroa, M. J., & Cornide, M. 1995a, A&AS, 114, 287
Montes, D., Fernandez-Figueroa, M. J., de Castro, E., & Cornide, M. 1995b, A&A, 294, 165
Morales, J. C., Gallardo, J. J., Ribas, I., et al. 2010, ApJ, 718, 502
Morales, J. C., Ribas, I., & Jordi, C. 2008, A&A, 478, 507
Morales, J. C., Ribas, I., Jordi, C., et al. 2009, ApJ, 691, 1400
Morin, J., Donati, J.-F., Petit, P., et al. 2008, MNRAS, 390, 567
Morin, J., Donati, J.-F., Petit, P., et al. 2010, MNRAS, 407, 2269
Morin, J., Jardine, M., Reiners, A., et al. 2013, AN, 334, 48
Muirhead, P. S., Hamren, K., Schlawin, E., et al. 2012, ApJL, 750, L37
Mullan, D. J., & MacDonald, J. 2001, ApJ, 559, 353
Neckel, H. 1995, SoPh, 156, 7
Nutzman, P., & Charbonneau, D. 2008, PASP, 120, 317
Orosz, J. A., Welsh, W. F., Carter, J. A., et al. 2012, ApJ, 758, 87
Parker, E. N. 1955, ApJ, 122, 293
Parker, E. N. 1979, Cosmical Magnetic Fields: Their Origin and Their Activity (New York: Oxford Univ. Press)
Pevtsov, A. A., Fisher, G. H., Acton, L. W., et al. 2003, ApJ, 598, 1387
Phan-Bao, N., Lim, J., Donati, J.-F., Johns-Krull, C. M., & Martín, E. L. 2009, ApJ, 704, 1721
Pineda, J. S., West, A. A., Bochanski, J. J., & Burgasser, A. J. 2013, AJ, 146, 50
Popper, D. M. 1976, IBVS, 1083, 1
Popper, D. M. 1980, ARA&A, 18, 115
Popper, D. M. 1997, AJ, 114, 1195
Qian, S.-B., Zhang, J., Zhu, L.-Y., et al. 2012, MNRAS, 423, 3646
Quirrenbach, A., Amado, P. J., Mandel, H., et al. 2010, Proc. SPIE, 7735, 773513
Reid, I. N., & Hawley, S. L. (ed.) 2005, New Light on Dark Stars: Red Dwarfs, Low-mass Stars, Brown Dwarfs, 2nd ed., Springer-Praxis Books in Astrophysics and Astronomy (Chichester, UK: Praxis Publishing Ltd)
Reid, I. N., Hawley, S. L., & Gizis, J. E. 1995, AJ, 110, 1838
Reiners, A. 2012, LRSP, 8, 1
Reiners, A., & Basri, G. 2007, ApJ, 656, 1121
Reiners, A., & Basri, G. 2009, A&A, 496, 787
Reiners, A., & Basri, G. 2010, ApJ, 710, 924
Reiners, A., Basri, G., & Browning, M. 2009, ApJ, 692, 538
Ribas, I. 2003, A&A, 398, 239
Ribas, I. 2006, Ap&SS, 304, 89
Ribeiro, T., Baptista, R., & Kafka, S. 2011, AJ, 142, 106

Richer, J., Michaud, G., & Turcotte, S. 2000, ApJ, 529, 338
Saar, S. H. 1990, in IAU Symp. 138: Solar Photosphere: Structure, Convection, and Magnetic Fields, ed. J. O. Stenflo (Cambridge: Cambridge Univ. Press), 427
Saar, S. H. 1996, in IAU Symp. 176, Stellar Surface Structure, ed. K. G. Strassmeier & J. L. Linsky (Dordrecht: Kluwer), 237
Saar, S. H. 2001, in ASP Conf. Ser. 223, 11th Cambridge Workshop on Cool Stars, Stellar Systems and the Sun, ed. R. J. Garcia Lopez, R. Rebolo, & M. R. Zapaterio Osorio (San Francisco, CA: ASP), 292
Schmitt, J. H. M. M., Fleming, T. A., & Giampapa, M. S. 1995, ApJ, 450, 392
Seager, S., & Mallén-Ornelas, G. 2003, ApJ, 585, 1038
Ségransan, D., Delfosse, X., Forveille, T., et al. 2000, A&A, 364, 665
Shulyak, D., Seifahrt, A., Reiners, A., Kochukhov, O., & Piskunov, N. 2011, MNRAS, 418, 2548
Skumanich, A. 1972, ApJ, 171, 565
Smith, M. A. 1974, ApJ, 189, 101
Spruit, H. C., & Weiss, A. 1986, A&A, 166, 167
Stassun, K. G., Kratter, K. M., Scholz, A., & Dupuy, T. J. 2012, ApJ, 756, 47
Stein, R. F., Brandenburg, A., & Nordlund, A. 1992, in ASP Conf. Ser. 26, Cool Stars, Stellar Systems, and the Sun, ed. M. S. Giampapa & J. A. Bookbinder (San Francisco, CA: ASP), 148
Stelzer, B., Burwitz, V., Audard, M., et al. 2002, A&A, 392, 585
Terrien, R. C., Fleming, S. W., Mahadevan, S., et al. 2012, ApJL, 760, L9
Torres, G. 2013, AN, 334, 4
Torres, G., Andersen, J., & Giménez, A. 2010, A&ARv, 18, 67
Torres, G., & Ribas, I. 2002, ApJ, 567, 1140
van Gent, H. 1926, BAN, 3, 121
van Leeuwen, F. 2007, A&A, 474, 653
Vida, K., Oláh, K., Kvári, Z., et al. 2009, A&A, 504, 1021
Voges, W., Aschenbach, B., Boller, Th., et al. 1999, A&A, 349, 389
Voges, W., Aschenbach, B., Boller, Th., et al. 2000, yCat, 9029, 0
von Braun, K., Boyajian, T. S., Kane, S. R., et al. 2012, ApJ, 753, 171
Vos, J., Clausen, J. V., Jorgensen, U. G., et al. 2012, A&A, 540, 64
Walkowicz, L. M., & Hawley, S. L. 2009, AJ, 137, 3297
Weis, E. W. 1991, AJ, 101, 1882
Weiss, A., Hillebrandt, W., Thomas, H.-C., & Ritter, H. 2004, Cox and Giuli's Principles of Stellar Structure (2nd ed.; Cambridge: Cambridge Scientific Publishers)
Welsh, W. F., Orosz, J. A., Carter, J. A., et al. 2012, Natur, 481, 475
Windmiller, G., Orosz, J. A., & Etzel, P. B. 2010, ApJ, 712, 1003
Winn, J. N., Albrecht, S., Johnson, J. A., et al. 2011, ApJL, 741, L1
Wright, E. L., Eisenhardt, P. R. M., Mainzer, A. K., et al. 2010, AJ, 140, 1868
Young, A., Skumanich, A., Stauffer, J. R., Harlan, E., & Bopp, B. W. 1989, ApJ, 344, 427
Zahn, J.-P. 1977, A&A, 57, 383